MECHANICAL PROPERTIES OF Aluminium-Magnesium-Silicon ALLOYS FOR AUTOMOTIVE AND AEROSPACE APPLICATIONS: A DENSITY FUNCTIONAL THEORY-BASED STUDY

Kipkorir Kirui Pius

A Thesis submitted to the School of Natural Sciences in partial fulfillment for the requirements of the degree of Master of Science in Physics of Masinde Muliro University of Science and Technology

SEPTEMBER, 2024

DECLARATION

This thesis is my original work prepared with no other than the indicated sources and support and has not been presented elsewhere for a degree or any other award.

Signature: ..... Date: .....

Kipkorir Kirui Pius

SPH/G/01-54018/2019

CERTIFICATION

The undersigned, certify that we have read and hereby recommend for acceptance of Masinde Muliro University of Science and Technology, this research thesis entitled, 'Mechanical Properties of Aluminium-Magnesium-Silicon Alloys for Automotive and Aerospace Applications: a Density Functional Theory-Based Study'

Signature: …….

Date: …….....

Dr. Maxwell Joel Mageto,

Department of Physics,

Masinde Muliro University of Science and Technology.

Signature: ..... Date: .....

Dr. Gaitho Magiri Francis,

Department of Physics,

Masinde Muliro University of Science and Technology.

Signature: ..... Date: .....

Dr. Ongwen Nicholas,

Department of Physics and Materials Science,Maseno University.

COPYRIGHT

ACKNOWLEDGEMENT

I acknowledge my supervisors, led by Dr. Mageto J. Maxwell, whose timely advice and continued support assisted immensely in the progress and completion of this work. His vast network and experience in research work helped in conceptualization of the work and resource mobilization (human and otherwise) to ensure the success of this study.

I thank Dr. Gaitho Francis for his tireless work in this work. His constant guidance and the hours he put made this work a success. His wide experience in supervision and research in computational Physics came in handy in the course of this study. His paper published with the MDPI, Polymers journal assisted us to get full waiver on our paper with the same publisher.

I will forever be indebted to Dr. Ongwen Nicholas for being an ever-present and ever-dependable supervisor in this work. He assisted a great deal in conceptualization of the work and was always available for consultation. His generosity enabled part of this work to be completed using his computational account at Center for High Performance Computing (CHPC) in South Africa. His diligence ensured that this work was completed on time with minimal errors.

I will also acknowledge Dr. Odari Victor for his timely pieces of advice that made this thesis as sound as it should be. His assistance, especially on revisions on the terms used, title and other scientific insights will not go unnoticed.

Lastly, I wish to acknowledge the CHPC in South Africa for their computational resources that made this work possible. The parallel computing available in their systems ensured faster attainment of results and hence, speeding up the work.

ABSTRACT

Aluminum and its alloys are utilized in various purposes, including aircraft skin, cookware, building cladding, train carriages, and electrical lines. This is attributable to their advantages, which encompass low density (physical density of 2.7g/cm^3, which is approximately a third that of steel), non-corrosivity, formability, good thermal and electrical conductivity, and availability. Moreover, its non-corrosivity diminishes with alloying. Several studies, mostly experimental, have been done on aluminum-magnesium-silicon (Al-Mg-Si) alloys (6xxx series). Mechanical properties, especially strength and ductility, have been explored in those earlier studies. However, other mechanical properties such as bulk modulus, shear modulus, Young's modulus, Poisson's ratio, Pugh's ratio, creep, and resilience have not been explored extensively. While this study touched on ductility and hardness, it also explored the bulk modulus, shear modulus, Young's modulus, Poisson's ratio, Pugh's ratio, and yield strength of Al-Mg-Si alloys. The main objective of this study was to determine the alloy composition that could yield stronger, harder, and more ductile materials that are appropriate for both aerospace and automotive industries by making use of density functional theory (DFT) calculations. The modeling of the structures was done using an aluminum cell as the starting structure, whose crystallographic information file was downloaded from the Crystallography.net website. It was then transferred to Burai software, where the unit cell was visualized and then transformed into 3 × 3 × 3 supercells containing 108 atoms, after which the supercells were alloyed with the appropriate number of Mg and Si atoms. Nine structures of Al-Mg-Si alloys with different percentages of Al, Mg, and Si were investigated. Structural optimization of the alloyed supercells was done as a preliminary to the study. The variable-cell relaxation was done using the Brodyden-Fletcher-Goldfarb-Shanno (BFGS) algorithm. The stress-strain method was employed in the calculation of elastic stiffness constants, from which mechanical properties were obtained. The elastic constants were calculated using Density Functional Theory (DFT) with the Perdew-Burke-Ernzerhof for Solids (PBESOL) functional, as implemented in the Quantum Espresso software. This work has conclusively demonstrated that the Si/Mg ratio is a pivotal determinant of the mechanical properties of Al-Mg-Si alloys. The optimal parameters identified in this study include a density of 2762 kg/m^3, a bulk modulus of 83.3 GPa, a shear modulus of 34.4 GPa, a Vickers hardness of 2.79 GPa, a Poisson's ratio of 0.413, a Pugh's ratio of 5.42, and a yield strength of 8.38 GPa. The ideal Si/Mg ratio for the majority of characteristics is 4.5. The alloys exhibiting these optimal features are suitable for industrial applications that necessitate such characteristics, including aircraft skins and mining equipment, particularly those with maximum hardness and yield strength. Their superior ductility enables their application in the fabrication of motor vehicle components and rail carriages. The alloys' low density renders them appropriate for manufacturing airplane components, as they enhance load capacity by minimizing part weight.

TABLE OF CONTENTS

LIST OF TABLES

LIST OF FIGURES

LIST OF ABREVIATIONS AND ACRONYMS

CIF	Crystallographic Information File
DFT	Density Functional Theory
FCC	Face-centered cubic
FFT	Fast Fourier Transforms
GP	Guinier Preston
VH	Vickers Hardness
HREM	High Resolution Electron microscope
PPs	Pseudopotentials
QE	Quantum Espresso
TEM	Transmission Electron Microscope

CHAPTER ONE

INTRODUCTION

1.1 Background of the study

Accidents often occur in planes, vehicles, and trains, leading to the loss of precious and productive lives. Approximately, 1.3 million people die each year as a result of road traffic crashes, 93% of which occur in low and middle-income countries (WHO, 2022). Kenya loses about 3000 people every year through road accidents, with motor vehicle accidents almost a daily occurrence. About 13000 people are injured, of which 6000 have serious injuries and need long-term medical treatments (Saidi & Kahoro, 2001). The most recent major plane crash in Africa is that of Ethiopian Airlines which occurred in Ethiopia shortly after take-off in March 2019. Though the initial report showed a software failure in the plane, it still would have been prevented if we had perfect materials that do not break even under high stress, and are also inflammable. (Gates, 2023)

Aluminum (Al) and its alloys have a wide range of applications as shown in Table 1.1. They range from cladding walls in buildings due to their attractive nature and non-corrodibility; aircraft parts due to their low density; power cables due to their high electrical conductivity and abundance, heat exchangers; and heat shields due to their superb thermal conductivity, just to mention but a few. Most car parts (up to 6% of its weight) such as gearbox housing, cylinder heads, and wheels are made of Al and/or its alloys. Aluminum and its alloys are preferred due to their many advantages such as low

density, relatively low cost, high thermal and electrical conductivity, as well as their corrosion resistance (Mageto, 2003).

Silicon (Si) on the other hand, is the second most abundant element on Earth's crust (Bruno & Nicholas, 2021). A number of investigations have been conducted on aluminum-magnesium-silicon (Al-Mg-Si) alloys. Al-Mg-Si alloys exhibit enhanced mechanical strength due to the formation of fine precipitates of Mg and Si from the solid-solution phase. The peak hardness results from a substantial quantity of coherent Guinier Preston 1 (GP1) zones (GP phase) and semi-coherent Guinier Preston 2 (GP2) zones (the Mg5Si6 phase, occasionally referred to as the β" phase), both of which manifest as needle-like structures (Derlet et al. 2009).

Table 1. 1: Some applications of aluminum and its alloys (Mageto, 2003)

Building	Transportation	Household
Cladding panels	Automotive trim	Baking trays
Roofing/ceiling	Heat exchangers	Cookware
Windows/doors	Cycles and invalid chairs	Domestic machines
Rainwater gutters	Motor cycles and mopeds	Furniture and office equipment
Roller shutter doors	Structural parts	Ladders
Floor heating	Heat shields	Vacuum cleaners
Insulation and ventilation	Air crafts	Lighting (surface products)
	High speed trains	Sports equipment

The principal constraint of aluminum is its low melting point (660 °C). Although mechanical strength can be enhanced via cold working and alloying, these methods often reduce corrosion resistance. The primary alloying elements are copper, silicon, magnesium, manganese, and zinc. A four-digit numeral that signifies the primary

impurities denotes the composition of Al, Mg, and Si. The categorization of aluminum alloys is presented in Table 1.2 (Mageto, 2003). In this method, a letter signifies the fundamental temper, while alterations to the temper are denoted by a number. Al-Mg-Si is classified within the 6xxx series of aluminum alloys, which incorporate minor amounts of elements including tin, indium, copper, iron, manganese, chromium, zinc, titanium, zirconium, and lanthanum, known to enhance the mechanical properties of this series (Baruah & Borah, 2020) (Yuan et al. 2012) (Werinos et al., 2016).

The microstructure, mechanical and thermal properties of Al-Mg-Si alloys have been studied by a number of researchers (Ambroziak & Solarczyk, 2018), however there is scanty literature on *ab initio* studies of a combination of mechanical properties namely bulk modulus, shear modulus, Youngs modulus, Poisson ratio, Pugh's ratio, Vickers hardness and ductility, of these alloys. Furthermore, the silicon and aluminium percentages used in this study have not been exhaustively explored in previous studies. Using density functional theory (DFT) (Lejaeghere, *et al*, 2016), various combinations of Al-Mg-Si alloys were modeled, and then their mechanical properties were calculated, with the main aim of optimizing them as regards to strength, hardness, and ductility as well as check the effect of Si/Mg ratio on these properties. DFT remains one of the most effective *ab initio* tools for quantitatively predicting and rationalizing the mechanical response of materials. In addition, DFT reduces the number of laboratory trials needed when manufacturing a material with desired mechanical properties (Kiely, *et al*. 2021). The choice of the alloys was made due to previous studies, which have shown that Al-Mg-Si alloys (6xxx series) are appropriate for use in the aircraft industry, motor vehicle

industry, and train manufacturing industry. It is worth noting that although the mechanical properties of the Al-Mg-Si alloys can be greatly improved by heat treatments, the same was not done in this study, since DFT calculations are carried out at the ground state.

Table 1. 2: Classification of aluminum alloys (Mageto, 2003)

Material	Designation
Aluminium of 99% minimum purity	1xxx
Aluminium copper alloys	2xxx
Aluminium manganese alloys	3xxx
Aluminium silicon alloys	4xxx
Aluminium magnesium alloys	5xxx
Aluminium magnesium silicon alloys	6xxx
Aluminium zinc alloys	7xxx
Miscellaneous alloys such as aluminium-lithium	8xxx

1.2 Statement of the problem

Aluminium and its alloys having so many applications have to be improved especially their microstructure and their mechanical properties. The challenge has always been to come up with materials with high resistance to cracking and spalling, owing to the rapid heating in the course of its use such as in aero planes, vehicles, and train coaches (Mageto, 2003). Under high stress, these materials should not break at a wide range of temperatures and should also not be easily flammable. Aircraft materials should also have very low density so as to reduce the weight of the aero plane parts and hence, increase the

load carried. This study therefore tries to solve the problem of cracking and spalling by improving the ductility and hardness of the Al-Mg-Si alloys through extensive alloying beyond the conventional percentages (<1%). The challenge with alloying Al is that it loses its ability to resist corrosion. The quest to find better materials is a continuous never-ending work. This study looked at various concentrations of Al, Mg, and Si that can give the best mechanical properties as regards strength, hardness, and ductility. It will also look at the Si/Mg ratio that yields optimum mechanical properties. These analyses on the alloys and their improvement will be done using DFT. The choice of the alloys in this study was due to previous studies that have shown that Al-Mg-Si alloys (6xxx series) are appropriate for use in the aircraft industry, motor vehicle industry, and train manufacturing industry. The alloys developed so far, though used in the industries, can still be improved in terms of strength, hardness, and even their melting points.

1.3 Objectives

1.3.1 Main Objective

The main objective of this study was to determine the alloy composition that could yield stronger, harder, and more ductile materials that are appropriate for both aerospace and automotive industries by making use of density functional theory calculations.

1.3.2 Specific Objectives

The specific objectives of the study were:

i. To model, using Burai software, the structures of aluminum-magnesium-silicon alloys at different concentrations of aluminum, magnesium, and silicon.
ii. To determine mechanical properties (bulk modulus, shear modulus, Young's modulus, yield strength, Poisson ratio, Pugh's ratio, and Vickers hardness) of the

modeled aluminum-magnesium-silicon alloys using density functional theory calculations (*ab initio* DFT).

iii. To investigate the effect of Si/Mg ratio (Si:Mg) on the mechanical properties of aluminium-magnesium-silicon alloys.

1.4 Justification of the study

Given the extensive applications of aluminum and its alloys, attention must be directed into the regulation of their structure and how this structure subsequently influences the mechanical properties of the alloys. This study is necessary, since there is need to improve the mechanical properties of the existing materials in order for them to meet the required industrial applications as well as to reduce accident fatalities that result from cracking and spalling of materials. Stronger and harder materials are still required in the aircraft, motor vehicle, and train manufacturing industries so as to reduce occurrence of accidents. Al-Mg-Si alloys are applied in rail coaches, truck frames, ship building, bridges, boiler making, hydraulic systems, mining equipment, pylons and towers, motorboats, framework for tents, rivets, and plane skins. Previous studies on these alloys have yielded materials that are not strong and hard enough, melt easily, and are also prone to stress corrosion cracking. Therefore, the need to look for ways of strengthening and improving the mechanical properties and of these alloys is justified. DFT employs open-source packages hence the budget will not involve acquiring of the software to be used. Modelling will reduce the resources used in experimental fabrication of the alloys since only those with the desired properties will be fabricated. This study tries to explore the effect of different concentrations of aluminum and its alloying elements with a view to giving a combination with the best mechanical properties. The resources required is

minimal and will go into good use since more resources will be required in the fabrication of these alloys. The research on mechanical properties of Al-Mg-Si alloys is relevant in this age of aircraft manufacture and endeavour for sustainable space exploration. The use of DFT in modelling and optimizing of the mechanical properties of these alloys will go a long way in reducing the costs of discovering appropriate materials for these purposes. This study is necessary so as to come up with stronger, more harder materials as well as materials with improved melting points appropriate for specific applications in both the aerospace and automotive industries. Mechanical properties can be predicted accurately using DFT calculations, especially for metal alloys and composite design.

1.5 Significance of the study

Aluminium and its alloys have desirable characteristics for use in various industrial applications. Specifically, Al-Mg-Si alloys have desirable mechanical properties which can be improved through alloying and heat treatments to make them even better for their industrial applications. The study of ways of optimizing their mechanical properties through alloying presents an opportunity for obtaining better materials for industrial uses such as plane skins, pylons and towers, rims of vehicle wheels, boilers, track frames and tent frames.

1.6 Scope of the Study

The study focused on Al-Mg-Si alloys alone. The alloys were modelled and their mechanical properties investigated using Density Functional theory (DFT) calculations. Nine alloys of aluminium (Al-Mg-Si alloys) with different concentrations of Al, Mg and

Si were investigated and their mechanical properties computed. In addition, a pure sample of aluminium was also studied for control purposes. This study did not touch on heat treatments (annealing and aging) of the alloys, but only focused on the influence of Si/Mg ratio as well as alloying on the mechanical properties of Al-Mg-Si alloys.

CHAPTER TWO

LITERATURE REVIEW

2.1 Introduction

This chapter looks at some of the previous work on Al-Mg-Si alloys. They are reviewed and the knowledge gaps are identified for investigation in the course of this study. The first section contains previous work on Al-Mg-Si alloys, which involves a detailed description of the various precipitates that are formed during the heat treatment of these alloys. The second section contains a description of DFT calculations. It describes what DFT calculation is all about and the equations and approximations that are involved. The third section gives explanations of the various mechanical properties of materials. The chapter concludes with the current applications of Al and its alloys.

2.2 Survey on Al-Mg-Si alloys

The mechanical characteristics of aluminum and its alloys have been the subject of several investigations. In order to better understand the hardening process, which is important for industry, Ninive et al. (2014) conducted a study on the β" phase, which is the main hardening precipitate in Al-Mg-Si alloys. They mixed advanced microscopy with *ab initio* atomistic calculations and strength measurements of Al-Mg-Si alloys that contained the β" precipitate. The strain fields within and surrounding the precipitates, as well as the energy required for their production, led microscopy to conclude that Mg4Al3Si4 was the most probable precipitate. The strain fields were quantified in the DFT computation using effective hardening radii instead of the observed radii.

Hardness cannot be accounted for by the quantity, percentage, or size of the precipitates, as the results also showed. The variation in hardness for comparable particle populations suggests that mechanical qualities are affected by other factors associated to particles. The tests conducted using HAADF-STEM on the β" structure most likely concluded that β" is composed of Mg5Al2Si4. Stabilities determined by density-functional theory (DFT) for various precipitate compositions seemed to contradict this, with Mg5Al2Si4 showing the highest stability followed by Mg5Si6 and Mg4Al3Si4. Nevertheless, according to Ninive et al. (2014), elastic contractions within the precipitates were predicted by DFT calculations, and anisotropic HAADF intensities indicated a greater Al concentration of Mg sites along the {130} interface. As a result, Al becomes more stable near the interface due to strain than it does within the precipitate itself. Improving the connection between the estimated and measured strength parameters was achieved by increasing the effective radius of the hardening precipitates by 1 nm. This allowed for the inclusion of the strain field in future developments of precipitate strengthening models. In contrast to that work, which solely considered Vickers hardness, the current investigation included bulk and shear moduli, Young's modulus, Poisson's ratio, Pugh's ratio, and Vickers hardness. According to Marioara et al. (2005), the hardness of Al-Mg-Si alloys is not caused by changes in the grain structure but rather by the production of precipitates. Additionally, it was discovered that Al alloys rich in Si and those rich in Mg react differently to aging. The alloys' hardness was determined to be low regardless of the Si/Mg ratio. The hardness peaks at a high level when the ratio from both sides approaches one, although the Mg side shows a much narrower peak breadth. After three hours, a dramatic initial peak appeared on the Si side. The high-resolution imaging (HREM) analysis linked this

peak to an abundance of tiny Guinier Preston (GP) zones in the shape of needles. Approximately 10–40 hours after increasing the annealing period, a second, broader hardness peak (plateau) appeared. In alloys that are rich in magnesium, the early peak is almost nonexistent and is substituted by a single peak that lasts for around 20 hours. This peak is created by the coarser needles of the β" phase. Hence, the strength in Si-rich alloys is due to both GP zones and β"; in Mg-rich alloys, on the other hand, β" is the primary precipitate. According to the study's findings, Si-rich Al alloys have a microstructure with very fine precipitates, which allows them to achieve high hardness with a very small volume percentage of precipitates. However, compared to Si-rich alloys, Mg-rich Al alloys exhibit a coarser microstructure and undergo overage at a faster rate. Hardness was the primary focus of the previous research, whereas ductility, yield strength, and Vickers hardness were the primary foci of the current investigation. On top of that, the previous study relied only on experiments, but the current one is computer-based.

Mageto (2003) investigated two distinct solution heat treatments (2 hours at 570 °C and 10 minutes at 520 °C) to examine the precipitation in 6xxx series (Al-Mg-Si) dispersoid-free alloys, employing a Transmission Electron Microscope (TEM) to analyze the grains and precipitates. The investigation demonstrated that the enhancement was exclusively attributable to precipitation particles, rather than grain size. Si-rich Al alloys exhibit optimal mechanical properties when subjected to a solution heat treatment at 520 °C for 10 minutes, followed by quenching and a 4-hour storage at room temperature, prior to aging at 175 °C for 3 hours. The material exhibited a hardness of 109 HV (1.069 GPa), a

yield strength of 219 MPa, a ductility of 11%, and an ultimate tensile strength of 251 MPa. The Si-rich alloy exhibited a highly refined microstructure. The enhancement in Vickers hardness, yield strength, and ductility was ascribed to the GP zones and β" phases.

Al-Mg-Si heat-treatable alloys exhibited a significant enhancement in hardness during the aging process. The enhancement in strength resulted from interface strain between the matrix and tiny semi-coherent metastable precipitates that formed from the solid solution (Mageto, 2003). The enhancement in the strength of these alloys resulted from the production of needle-like precipitates, rather than alterations in grain size. The precipitation phases included the GP zones, β", β', U1, U2, B, β, and silicon phase. The most robust precipitates were generated during the β" phase. While the other phases enhanced the alloy's strength, their strengths were comparatively inferior to that of the β phase. Moreover, Si-rich alloys generally possess a finely precipitated microstructure. The enhancement in hardness, yield strength, and ductility of the alloys was ascribed to the GP zones and β" phases. The hardness was ascribed to the interface coherency in the {001} type Al planes, which generated robust strain fields around the precipitates, hence impeding dislocation migration. The dimensions of the new grain are contingent upon the solution heat-treatment temperature and the duration of annealing.
The grain size was seen to grow with prolonged annealing time and elevated solution heat-treatment temperature. The yield strength was determined to be contingent upon the Si/Mg ratio, particularly at shorter annealing durations. A higher ratio indicates superior yield strength. At reduced annealing durations, yield strength is also contingent upon the temperature of the solution heat treatment. A reduced solution treatment temperature

correlates with enhanced yield strength. Ductility is somewhat contingent upon the Si/Mg ratio; a higher ratio correlates with enhanced ductility. This is applicable solely for reduced annealing durations. Reduced volume fractions are advantageous for enhanced yield strength. The research concentrated on a restricted concentration of aluminum, magnesium, and silicon across two alloys. The current investigation encompasses a broader concentration range, consisting of nine alloys. Furthermore, the previous work was exclusively experimental, whereas the current study is entirely computational.

Bonding between Al-Mg-Si and Mg-Si compounds was investigated by Froseth et al. (2003), which is pertinent to Al-Mg-Si alloys. The stability and bonding were studied by means of (linearized) augmented plane-wave + (local orbitals) DFT computations. In the precipitation sequence, they demonstrated that the β and β" phases were defined by the existence of covalent connections between Si-Si nearest-neighbor pairs and Mg-Si nearest-neighbor pairs. The final equilibrium structure of the precipitation series was the β phase, which is fluorite Mg2Si. The unit cell was a primitive face-centered cubic (fcc) type, belonging to the space group Fm3m and having 225 dimensions, while the experimental lattice parameter was 6.39 Å. It produced particles with a cubic or plate-like structure with a diameter of up to 20 μm. Completely disorganized was its interaction with the Al matrix. A monoclinic conventional unit cell (space group C2m) with experimental lattice parameters a=15.16 Å, b=6.74 Å, c=4.05 Å and γab=105.30 was present in the β" phase. In its most common form, this phase produces needle-shaped precipitates that range in length from 300 to 400 Å and thickness from 30 to 50 Å. In the β"-phase unit cell, the needle length was along the {001} direction; in the Al matrix, it

runs parallel to the {001} direction. The trigonal U1 conventional primitive cell, which belonged to the Al-Mg-Si phases and was in space group P3m1, had lattice parameters a=b=4.05 Å and c=6.74 Å, as determined experimentally. Its formula was MgAl2Si3, which derived from the elements magnesium, aluminum, and silicon. The {001} direction of the U1 unit cell is found to run parallel to the {310} direction of the fcc Al matrix, according to the experiments. The rod-shaped precipitates that the U1 phase produced had a width of around 50 nm and a length of 50-500 nm. The experimentally determined unit cell volume and the computed unit-cell equilibrium volume differed by a mere 1% after a volume-relaxation. A bulk modulus of 71 GPa was found from the fitting using the second-order Birch-Murnaghan equation of state.

The orthorhombic space group Pnma unit cell U2 had lattice parameters a=6.75 Å, b=4.05 Å, and c=7.94 Å, which were determined experimentally. With a formula of Mg4Al4Si4, it consisted of four magnesium atoms, four aluminum atoms, and four silicon atoms. In most cases, the U2 phase will produce a precipitate that is identical in size and shape to the U1 phase. A parallel orientation between the {310} direction of the fcc Al matrix and the {100} direction of the unit cell was discovered. The equilibrium volume, which was obtained by relaxing the unit cell's volume, differed from the experimentally determined unit-cell volume by less than 1%. The bulk modulus of 69.1 GPa, as determined using a second-order Birch fit, is highly similar to the value found for the U1 phase. Table 2.1 (Froseth et al., 2003) displays the results of the calculations of formation energy and bulk moduli for different precipitation phases. The β'' and β' phases had positive formation energies, indicating that formation energy is absorbed

(endothermic) during their production. In contrast, the β, U1 and U2 phases had negative formation energies, indicating that energy is lost (exothermic). Phases two and three have greater bulk moduli than phases one and two. The bulk mechanical characteristics of the entire crystal and the impacts of the Si/Mg ratio on these alloys are examined in the present work, in contrast to Froseth and group's investigation, which primarily concentrated on the bonding and bulk modulus of the precipitates generated.

.

Table 2. 1: The formation energies and bulk moduli of space groups given with space group numbers in parentheses (Froseth et al., 2003)

Structure	Space group	Al-Mg-Si ratio	Lattice parameter (Å)	Bulk modulus (GPa)	Formation energy (mRy)
β'	C2/m (12)	0:5:6	a = 15.16 b = 6.74 c = 4.05	65	3.53
β	Fm3m (225)	0:4:2	a = b = c = 6.39	54	-10.93
β'Matsuda	P62m (189)	0:4:2	a = b = 7.1 c = 4.05		38.174
U2	P3m1 (164)	4:4:4	a = b = 4.05 c = 6.74	69	-3.04
U1	Pnma (62)	2:1:2	a = 6.75 b = 4.05 c = 7.94	71	-0.45

Marioara et al. (2005) investigated six Al-Mg-Si alloys (6xxx series) with varying percentages of Mg and Si. The samples were aged for several durations, and their

mechanical properties were examined. The established precipitation sequence in the Al-Mg-Si alloy system is: SSSS → atomic cluster containing Mg, Si → GP1 zones → GP2 zones (β^") → β^' → β, where SSS denotes the initial supersaturated solid solution. The β" phases are presumed to be devoid of Al, although this is not confirmed. Typically, during heat treatment, the subsequent phase formed is more enriched in Mg than its predecessor. Table 2.2 delineates the recognized periods of precipitation.

Table 2. 2: Overview of known precipitation phases in Al-Mg-Si; U1, U2, and B', are also called A, B and C (Marioara, Andersen, et al., 2005)

Phase	Shape	Compound	Space Group	Lattice Parameters
GP zones	Needle	Unknown	C2/m	a=1.48, b=0.405, c=0.648, β=105.3
β'	Needle	$Mg_{1.8}Si$	$P6_3$	a=0.715 b=0.405 ϒ=120
U1	Needle	$MgAl_2Si_2$	P_3m_1	a=b=0.405 c=0.674, ϒ=120
U2	Needle	MgAlSi	P_nm_a	a=0.675, b=0.405, c=0.794
B'	Lath	Unknown	Hexagonal	a=1.04, c=0.405, ϒ=120
B	Plate	Mg_2Si	F_m3_m	a=0.6354
Si	plate	Si	F_d3_m	a=0.5431

Most of the above previous studies on Al-Mg-Si alloys are experimental. This study was purely computational. All the alloys were modelled and the concentrations presented here had not been investigated before. Also, while the previous studies investigated strength and hardness only, this study explored other mechanical properties such as Young's modulus, bulk modulus, shear modulus, Pugh's ratio and ductility.

2.3 Density functional theory calculations

Densely Functional Theory employs a series of rational physical approximations to reduce the many-particle Schrödinger equation to a form that is numerically solvable (Lejaeghere et al., 2016). Equation 2.1 presents the many-particle Schrödinger equation.

(2.1)

where is the many-particle wave function for N particles, where each particle has its own mass m_i, charge z_i, and position r_i. The interaction is the coulomb interaction: is the kinetic energy of the N particles, and is the total potential energy of the N particles. DFT computations utilize the Born-Oppenheimer approximation alongside a suitable functional selection. The Kohn-Sham equations facilitate the determination of the ground state energy and electronic density of a system comprising interacting electrons and ions.

2.3.1 Born-Oppenheimer approximation

The initial approximation stems from the physical problem under investigation: the ground state of interacting ions and electrons. Given that even the lightest ion exceeds an electron's mass by over a thousandfold, we can disregard the dynamics of ions entirely. This is referred to as the Born-Oppenheimer approximation (Born & Oppenheimer, 1927). The time-independent Schrödinger equation for a system of N electrons influenced by the electron potential generated by stationary ions can be expressed as:

(2.2)

where the potential $V(r_i)$ is created by the charged ions:

$V(r_i) =$, (2.3)

where R is the (static) positions of the ions; and z_j is their charge.

The electronic density is obtained by integrating all electron degrees of freedom, except one,

(2.4)

The total potential energy V is just given by the integral over the potential V(r) times the density.

(2.5)

2.3.2 Hohenberg-Kohn theory

Assume we have determined the solution to equation (2.2), yielding a ground state energy E0 and a specific electronic density n(r) (Kohn & Sham, 1965). The magnitude of the Coulomb interaction and the mass of an electron are fundamental constants of nature. The sole factor that can potentially affect the electronic density n(r) and the ground state energy E0 is the selection of the voltage V(r). The ground state is a functional dependent on the input potential.

(2.6)

An additional function can be passed as an argument to a functional. An independent functional for the potential, kinetic, and interaction energies allows us to express the ground state energy as:

(2.7)

An elegant realization by Hohenberg and Kohn is that the electronic density n(r) and the potential V(r) are conjugate variables. Equation (2.7) can be modified such that it is dependent on density n(r) instead of potential V(r):

(2.8)

Two minor problems exist: the functional's appearance is unknown, and even if it were known, determining the appropriate electrical density is a hurdle.

.

2.3.3 Approximating the functional

The unspecified functional F[n(r)] must characterize the kinetic and interaction energy of the system delineated by equation (2.2). Although we cannot ascertain its precise shape, we examine its form in certain solvable limiting instances. A free homogeneous electron gas with density n and mass m possesses a ground state energy of:

(2.9)

The kinetic energy contribution to the entire functional F[n(r)] for a slowly fluctuating electron density can be approximated by evaluating the energy in equation (2.9) at each position separately:

(2.10)

In addition, the Hartree term provides the minimum energy contribution from coulomb interactions, as is known from perturbation theory:

(2.11)

The whole Hohenberg-Kohn functional, encompassing the potential energy, is as follows:

(2.12)

where E_{xc} is the exchange correlation potential (very small).

2.3.4 Kohn-Sham equations

The appropriate n(r) is identified, as it minimizes the functional. The functional can be determined by equating its derivative to zero:

(2.13)

Employing the functional in equation (2.12), we obtain:

(2.14)

Essentially, Kohn and Sham wanted to approach this problem as if it were a problem involving only one particle. Kinetic energy is denoted by the first term, and the Kohn-Sham potential is formed from the other terms:

(2.15)

Equation (2.16), which represents the potential, is part of the Kohn-Sham equation, which is a Schrödinger equation for a single particle.

((2.16)

Equation 2.16 can be solved numerically, as it is a linear differential equation, making it manageable. The electron density is derived by populating the N solutions ψ_i (r) corresponding to the lowest energy levels.

(2.17)

The electron density derived in this manner can be utilized to compute a new Kohn-Sham potential, in accordance with equation (2.15). We persist with this repeated process until convergence is achieved. In the above derivation, we entirely disregarded the spin of the electrons. Indeed, actual electrons possess spin, necessitating the inclusion of that degree of freedom as well. Nonetheless, this does not alter any essential aspects of the application of Kohn-Sham equations.

2.4 Mechanical properties of materials

2.4.1 Mechanical strength

The resistance of a material to deformation under the influence of an external force is known as its mechanical strength (Marie, 2021). A material's mechanical strength is directly proportional to its ability to resist external loading. There are two areas where mechanical strength can be defined according to the amount of deformation: yield strength and ultimate strength. In contrast to ultimate strength, which is the maximum load that a material can endure before breaking, yield strength shows the maximum load that a material can endure within its elastic limit. Solids exhibit both of these qualities. As a unit of measurement, mechanical strength is N/mm^2. Therefore, it is consistently expressed as a unit of area. The mechanical strength of a material can be found by using a universal testing machine to conduct standard tensile or compressive tests.

2.4.2 Hardness

A material's hardness is defined by how well it withstands impact from other materials, such as scratches, indentations, or penetrations (Marie, 2021). One way to quantify hardness is by comparing it to some other substance. It never applies to the inside of a solid, only its surface. It is possible for a tougher substance to permeate a softer one. There are a variety of hardness scales, each with its own unique indenter. The capacity of a conventional indenter to make an indentation or scratch on the surface of the workpiece is evaluated while hardness is being measured. Harder materials are more resistant to wear and scratching, which means they are also better at withstanding mechanical wears like erosion and abrasion. The Rockwell, Brinell, Vickers, and Shore scleroscope are some of the many ways that hardness can be measured. The study used Vickers hardness as its metric.

A Matsuzaw DVK-1S method can be used to experimentally quantify Vickers hardness. The 1 kgf load, 100 μms loading speed, and 15 s pressing time were all utilized. A tiny pyramidal indenter with a square base and an included face angle of 1360 is pressed into a surface of a sample (figure 2.1). A unitless hardness number, HV, and the resultant impression, diagonals d1 and d2, as assessed under a light microscope, were automatically calculated using equation 2.18.

, 2.18

Where P represents the weight in kgf, d is the mean diagonal imprint in mm, and α signifies the face angle dimension, which is 1360.

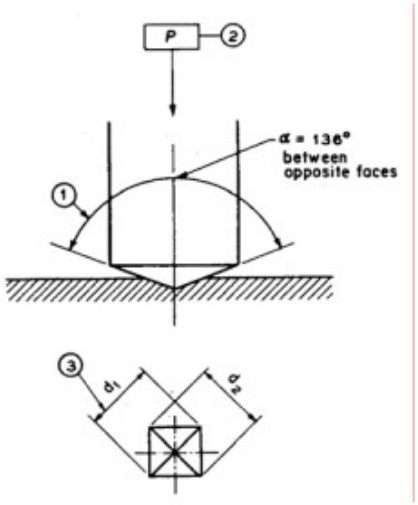

Figure 2. 1: Vickers Hardness measurement

2.4.3 Elastic constants

A number of elasticity constants are included. Moduli such as Young's, bulk, shear, and Poisson's ratio are examples of such. The tensile elasticity along a line when two opposing forces are applied is described by the Young's modulus. As an alternative, the bulk modulus is the three-dimensional version of the Young's modulus. Volumetric elasticity, defined as the ratio of volumetric stress to volumetric strain, is a useful quantity to have on hand. A material's bulk modulus is a constant that indicates its compressive strength. The change in volume as a function of increasing pressure is called viscosity (Marie, 2021).

Bulk Modulus = Volumetric Stress/ Volumetric Strain

=

= (2.18)

in which P1 and P0 denote the ending and beginning pressures, V1 and V0 the ending and beginning volumes, and ρ_1 and ρ_0 the ending and beginning densities, respectively. A material's bulk modulus is a constant that indicates its compressive strength. The SI unit for the bulk modulus is either pounds per square inch (PSI) in the Imperial system or pascal (Pa) in the metric system.
When two forces acting on an object cause it to shear, the result is described by its shear modulus (G), also called its modulus of rigidity. Substituting shear strain for shear stress yields the shear modulus. Pascal is the SI unit of work. To find the shear modulus, one must measure the deformation of a solid under the action of a force parallel to one of its surfaces, with another force acting on the opposite surface to keep the solid in place. A solid's rigidity is shown by its substantial shear modulus value. Thus, a substantial amount of force is necessary for its deformation. A solid is soft or flexible with a small shear modulus value, meaning it takes minimal force to deform it.
The ratio of the bulk modulus to the shear modulus is known as Pugh's ratio (B/G). When comparing the strains caused by transverse contraction and longitudinal extension, it can be useful. One way to estimate a material's ductility or brittleness is using Pugh's ratio. In addition, the Vickers hardness can be determined using the Chen model (Chen, Niu, Franchini, Li, & Li, 2011).

2.4.4 Elastic Anisotropy

Isotropy is the property of a material, which relates to the stress and strain in the material. Anisotropy occurs when the orientation of a material affects the relationship between stress and strain in that material. If the applied stress is rotated, the response of the material to strain will differ.

CHAPTER THREE

MATERIALS AND METHODS

3.1 Introduction

In this chapter, the simulation techniques used in the study of Al-Mg-Si alloys are described in detail. This entails how the alloys were modelled by first downloading the Al crystallographic information file (CIF) from the Materials Project website, then visualizing the crystal cell in the Burai software before creating 3×3×3 supercells, then alloying the supercells with the required number of atoms of the alloying elements. It also involves how the input file was generated from the Burai software, then how it was transferred to the quantum espresso (QE) software. It also involves how DFT calculations were done on the modelled supercells. It also includes a brief discussion on pseudopotentials and how they are chosen. Structural optimization is described and lastly, the determination of various mechanical properties are described, together with the formulae used to calculate them.

3.2 Crystal structure for input

The alloys were modeled by downloading a CIF file of Al from Crystallography.net. The downloaded file was of Fm3m, space group number 225, lattice parameter 4.0478 Å (Franco *et al* 2006). Al has an electronic configuration of $1s^2 2s^2 2p^6 3s^2 3p^1$.

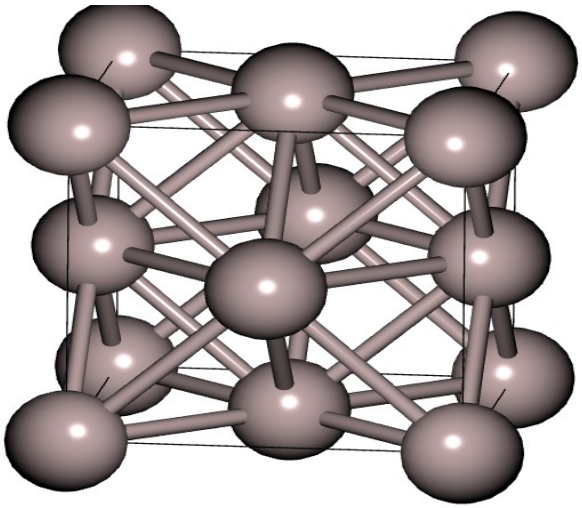

Figure 3. 1: The aluminium unit cell as visualized by Burai, a tool for crystal structure visualization as well as input file generation

The CIF file was then transferred to the Burai tool and the crystal cell (FCC) containing 4 atoms was first transformed into a 3 × 3 × 3 supercell containing 108 atoms, with lattice parameter of 12.1434 Å to allow for substitution of whole number atoms during alloying. The supercell was then alloyed by replacing some of the Al atoms with those of Mg and Si atoms as per the concentrations given in table 3.1. This was done within the Burai interface. (Ongwen *et al*, 2020)

Table 3. 1: Concentrations of various Al-Mg-Si under study and the number of atoms of each element

Sample ID	Silicon		Magnesium		Aluminium		Si/Mg ratio
	Conc. (%)	Atoms	Conc. (%)	Atoms	Conc. (%)	Atoms	
A_00	0	0	0	0	100	108	-
A_19	1	1	9	10	90	97	0.100
A_28	2	2	8	9	90	97	0.222
A_37	3	3	7	8	90	97	0.375
A_46	4	4	6	7	90	97	0.571
A_55	5	5	5	5	90	97	1.000
A_64	6	7	4	4	90	97	1.750
A_73	7	8	3	3	90	97	2.667
A_82	8	9	2	2	90	97	4.500
A_91	9	10	1	1	90	97	10.00

The Sample ID used in table 3.1 contains the silicon percentage concentration (first digit), followed by the magnesium percentage concentration (second digit). For example, the alloy with the code name A_28 (A stands for alloy) has 2% silicon atoms and 8% magnesium atoms. The choice of concentrations was such that the percentages used give the number of atoms in the supercell that is approximately a whole number. This was then rounded off to the nearest whole number, since the number of atoms is always a whole number. The concentration of Al was kept constant at 90%, while that of Si and Mg were varied to yield the nine Al alloys with the different concentrations which was sufficient in comparison and establishment of trends. The first alloy had the lowest concentration of Si (1%) and the highest concentration of Mg (9%). Si concentration was

then increased, while that of Mg was reduced. Figure 3.2 shows the 3D structures of the alloyed supercells of all the nine Al-Mg-Si alloys.

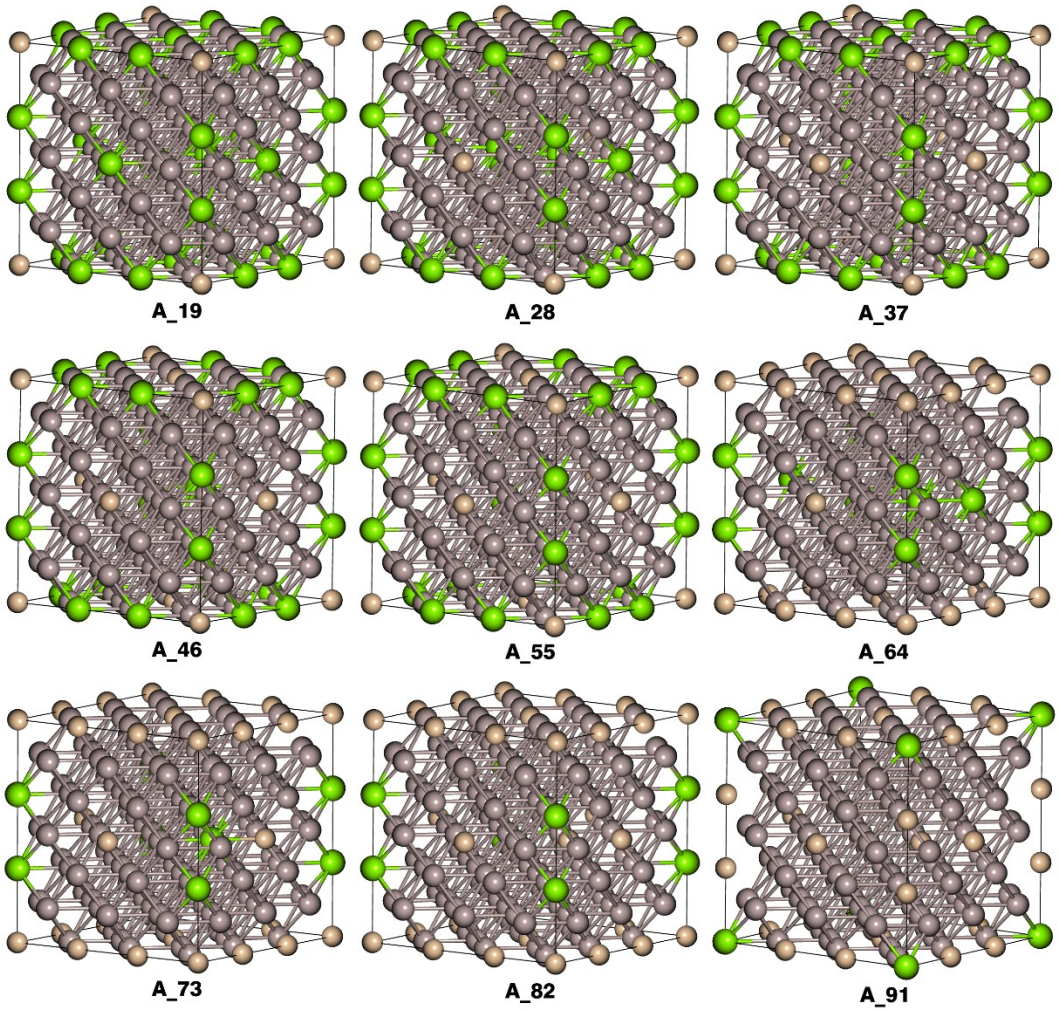

Figure 3. 2: Supercells of the modelled Al-Mg-Si alloys. (Al atoms (grey), Si atoms (yellow) and Mg atoms (green))

3.3 Choice of pseudopotentials

This computational study employs DFT, which resolves the Kohn-Sham equation, essentially a one-electron Schrödinger equation for a hypothetical system of non-interacting particles that produces the same density as any specified system of interacting

particles (Kohn & Sham, 1965). The resolution of Kohn-Sham equations is achieved by Density Functional Theory (DFT) via an iterative process known as self-consistent field (SCF) calculation. The quantity of SCF cycles executed prior to achieving convergence (self-consistency) is contingent upon the material being analyzed (including factors such as atomic quantity, crystal structure, and atomic molecular masses) and the convergence parameters (such as the convergence threshold).

The computational features of materials in Quantum Espresso (QE) necessitate pseudopotentials (PPs) as inputs. A pseudopotential (PP) seeks to substitute the intricate interactions of core electrons and nuclei with an effective potential, thereby modifying the Schrödinger equation to include an effective potential term in place of the conventional Coulombic potential term for core electrons (Naturfosch, 1977). In a PP, the core states are removed, and the valence electrons are represented by pseudo wave functions with reduced nodes. Consequently, plane-wave basis sets can efficiently describe pseudo-wave functions with a reduced number of Fourier modes. For first-principle pseudopotentials to be calculated from an atomic reference state, it is essential that the pseudo and all-electron valence eigenstates exhibit identical energies, amplitudes, and densities beyond a designated core with a cutoff radius, rc. Larger cut-off radii are expected to render pseudopotentials softer (converge rapidly), however they exhibit less transferability (Schwerdfeger, 2011).

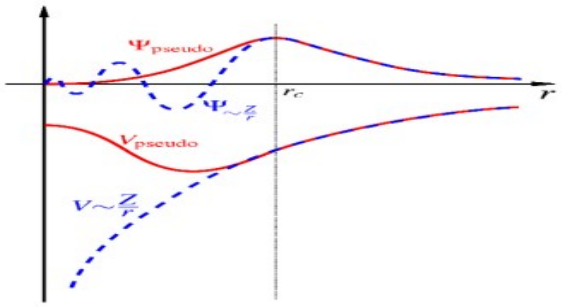

Figure 3. 3: A wave function in the nucleus' Coulomb potential (blue), and in the pseudopotential (red). Above the cut-off radius rc, the Coulomb and pseudo wave functions potentials coincide.

This study characterized electron-ion interactions using scalar-relativistic, norm-conserving ultrasoft pseudopotentials. Ultrasoft pseudopotentials permit the utilization of a basis set with a markedly lower kinetic energy cutoff (ecut) for the representation of electron wave functions, facilitating numerical convergence with manageable computational resources. Additionally, they alleviate norm-conserving constraints, thereby diminishing the requisite basis set size, albeit at the cost of introducing a generalized eigenvalue problem (Vanderbilt, 1990). The Perdew-Burke-Ernzerhof functional for solids (PBESOL) was employed, as it produces mechanical property results that are equivalent to experimental data.

Norm-conserving ultrasoft pseudopotentials (PPs) by Adllan & Corso (2011): *Al.pbesol.rrkjus.UPF*, *Mg.pbesol.rrkjus.UPF* and *Si.pbesol.rrkjus.UPF*, which have been generated with scalar-relativistic calculation, were employed. PBESOL PPs produce results for mechanical properties that are comparable to those of experiments (Ongwen, Ogam, & Otunga, 2020). Furthermore, ultrasoft pseudopotentials permit the utilization of basis sets with a markedly reduced kinetic energy cut-off (ecut) for characterizing the electron wave function, hence facilitating numerical convergence with adequate

computational resources. Moreover, ultrasoft pseudopotentials alleviate the norm-conserving requirements, hence diminishing the requisite basis-set size, but at the cost of introducing a generalized eigenvalue problem.

3.4 Structural optimization

In this study, the kinetic energy cut off (ecut), charge density cut off (ecutrho) (ecut×8), k_ points and the lattice parameters were optimized. Ecut was varied from 10 to 100 in steps of 10, leading to 10 data points. A graph of total energy against ecut was then plotted in order to attain the optimum point. The structural optimization was achieved when the difference between two adjacent values of total energy was in the order of 10^{-4} Ry. The optimum ecut value found was taken to the next stage in optimization of k_points. K_points were varied from 2 to 9 in steps of 1, yielding 8 input files. A graph of total energy against k_points was then plotted in order to obtain the optimum k_point. The optimum k_point found together with optimum ecut were taken to the next stage to optimize the lattice parameters. Calculations on total energy were conducted to determine the equilibrium lattice parameter of the crystal by altering the lattice parameters in increments of 0.2 a.u. throughout a range of unit cell volumes from 19.3 to 22.1, resulting in 15 data points. A graph depicting total energy versus lattice parameters was constructed to determine the optimal lattice parameter. The equilibrium lattice parameters were derived by fitting the total energies against volumes data to the third-order Birch-Murnaghan equation of state, as presented in equation 3.1 (Katsura et al., 2019).

(3.1)

given that P=pressure, Vo=reference volume, V=deformed volume, B0=bulk modulus, and B0'=derivative of bulk modulus with respect to pressure. Equation 3.1 was used to get the minimal parameters for the equilibrium cell. Equation 3.2, which gives the volume of a cubic cell, was then used to calculate the values of the equilibrium cell parameters.

(3.2)

Following the optimization of the lattice parameters, the atomic coordinates were refined by a variable cell relaxation calculation (vc-relax) utilizing the BFGS method, ensuring that the force components on each atom are below ×10^-4 Ry/Å.

3.5 Determination of mechanical properties

Materials' elastic properties reveal crucial information about a compound's structural stability, bonding characteristics between neighboring planes, and the anisotropic nature of bonding. In order to determine a material's elastic constant, one must be familiar with the strain-energy curve curvature for the chosen deformations (Munjal et al. 2011). It is common practice to use three separate elastic stiffness constants, c11, c12, and c44, when calculating the elastic constants of a basic cubic cell using energy-strain analysis (Ravindran, 1988). A crystal's resistance to deformation under external force is measured by its elastic stiffness constant, abbreviated as cij. An expected quadratic dependence of the elastic energy with the tensor of deformation (Hooke's law) is anticipated for minor deformations (Landau & Lifshitz, 1970).

Ravindran et al. (1988) state that the internal energy of a strained crystal can be expressed as a Taylor expansion in terms of the strain tensor, relative to the initial internal energy of the unstrained crystal as follows:

, (3.3a)

In this context, E (V, δ) denotes the total energy of the strained system, while E (Vo, 0) signifies the total energy of the unstrained system. Here, V_o represents the volume of the unstrained system, η is the Lagrangian coordinate, and cij indicates the second-order elastic stiffness constants in Voigt notation, where the indices ij are substituted with 1, 2, 3, 4, 5, and 6 corresponding to xx, yy, zz, yz, xz, and xy, respectively. The Taylor expansion of the total energy is expressed in Lagrangian coordinates η, which are related to the Eulerian coordinates δ by the equation . Given that δ is minimal, the approximation η = δ holds true. Reorganizing equation 3.3a and substituting η with δ yields:

(3.3b)

where the quantity is called the energy density.

Three distinct strains are required to ascertain the three separate elastic stiffness constants of a cubic cell. The three elastic stiffness constants (c_11, c_12, and c_44) are derived from the distortion matrices D_1, D_2, and D_3, respectively. The distortion matrix for C11 is expressed as:

(3.4a)

In the distortion matrix D1, the symmetry of the deformed lattice remains cubic. Nevertheless, the cell's volume is altered. The energy related to the distortion is derived by substituting the strain matrix values into equation 3.3b and excluding the third-order term to yield:

(3.4b)

The shear elastic stiffness constant (c_44) can be determined by employing the volume-conserving monoclinic shear distortion as follows:

(3.5a)

The energy associated with the distortion (D_2) can be expressed as:

(3.5b)

The residual elastic stiffness constant (c_12) is subsequently computed by a volume-conserving orthorhombic distortion of the following type:

(3.6a)

The energy related to the distortion (D_3) is subsequently derived by substituting the strain matrix values into equation 3.3b to yield:

(3.6b)

The 13 data points were subjected to strains of ±0.025 in increments of 0.005. According to (Wen, et al., 2017), there is a relationship between the elastic compliance constants (Sij) and the elastic stiffness constants (cij):

(3.7)

The three elastic stiffness constants C_{ij} must meet the Borne Huang criterion for a stable supercell (Boucetta & Zegrar, 2013),

$$C_{11}>0;\ C_{44}>0,$$

$$C_{11}-C_{12}>0;\ 2C_{11}-2C_{12}>0,$$

$$2[(C_{11}+C_{12})+(C_{11}+4C_{12}]>0 \qquad (3.8)$$

According to Bouchonafa et al. (2020), solids are able to withstand stresses that would otherwise cause them to distort. The characteristics of a material's response to external loads, as given by its elastic properties, can be used in several ways. Hooke's rule governs the elastic properties of materials. It asserts that stresses σi in a material are precisely proportional to the applied strain δj within the crystal's linear regime.

(3.9)

In this study, the stress-strain method by Ongwen, Ogam & Otunga (2020) was employed, where the energy-strain by Ravindran *et al.* (1988) was modified. In the stress-strain method, only two distortions (and) are required as opposed to the three for the energy-strain method.

The crystal was subjected to small strains in order to stay within the linear range of Hooke's law (<1%). There were a total of 7 data points in each calculation, with stresses

applied in increments of 0.0025, resulting in ± 0.0075. Using the SCF calculation output files on the distorted cells, we can determine D1's elastic stiffness constants, c11 and c12, and D2's C44 in the following ways: c11 from D1's first element of the stress matrix (xx), and C12 from D1's middle element (yy). Figure 3.3 shows that c44 was derived from the final element (zz) of D2 (Ongwen et al., 2020).

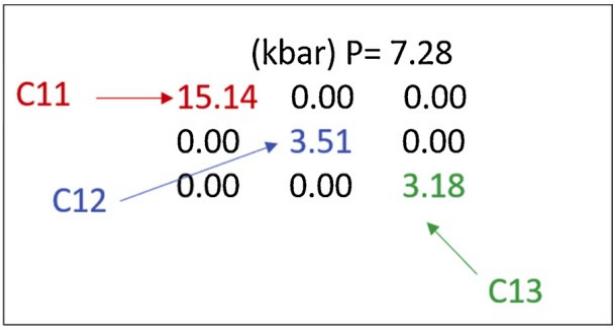

Figure 3. 4: A section of the output of SCF calculation, showing the stresses on the crystal for D1. The elastic stiffness constants c11 and c12 are read from the matrix as shown (Ongwen, Ogam, & Otunga, 2020)

The Voigt and Reuss approximations were used to derive the bulk modulus (B) and the shear modulus (G) using the elastic stiffness (cij) and elastic compliance constants (sij). In a basic cubic crystal, the Voigt bulk modulus (Bv) and shear modulus (Gv) are defined as follows:

(3.10a)

(3.10b)

The Reuss bulk modulus (BR) and the shear bulk modulus (Gv) are defined as follows:

(3.11a)

(3.11b)

The elastic compliance constants (S_{ij}) are obtained according to the relations:

(3.12a)

(3.12b)

(3.12c)

Calculated as Hill's average, which is defined as the geometric mean of the Voigt and Reuss moduli and provided as follows (Hill, 1952):

(3.13)

The brittle and ductile behavior of a material was determined by using equation 3.14 (Wen *et al*. 2017):

(3.14)

where n is a constant known as Pugh's modulus ratio. If n>1.75, the material is ductile. Otherwise, the material is brittle.

The Chen model was used to determine Vickers hardness (Hv) (Chen, Niu, et al., 2011).

(3.15)

Additionally, Avery et al. (2019) utilized the Tian model, which can be found in equation (3.16), for the purposes of comparison and improvement.

(3.16)

where n is the Pugh's ratio and G is the shear modulus.

Yield strength was calculated using the formula:

(3.17)

To determine the elastic anisotropy of the alloys, anisotropic factor (A) was calculated using the formula in equation 3.17 (Zener, 1948),

(3.18)

There is a correlation between the alloy's A and its twistability. An isotropic material has an A value of 1, whereas an anisotropic material has an A value of less than or greater than 1.

CHAPTER FOUR

RESULTS AND DISCUSSION

4.1 Introduction

This chapter deals with the results obtained from this study and their interpretations. The chapter starts by describing the results from structural optimization; including optimization of ecuts, K_points, and the lattice parameters for the sample alloys. The elastic stiffness constants obtained from the stress-strain curves, as well as the mechanical properties of the alloys are presented and discussed. Moreover, the variation of Si/Mg ratio on the mechanical properties is presented and discussed. Finally, the anisotropic constant is discussed together with its implications.

4.2 Structural Optimization

Figures 4.1a and 4.1b show the variation of the total energy per atom with ecut for all the alloy samples in this study individually in figure 4.1a and combined in figure 4.1b. From the figures, the ecut was observed to stabilize at 50 Ry. Thus, 50 Ry was picked for the subsequent calculations for all the supercells. The energy difference between the 55 Ry

and 50 Ry total energies was found to be 2.4 x 10^{-3} Ry, confirming 50 Ry to be the optimum ecut. Presented in figure 4.2 is the total energy per atom against K_points, also for all the alloys in this study, which was found to stabilize at the 5 x 5 x 5 mesh. The energy difference corresponding this mesh was found to be 3.5 x 10^{-4} Ry. Hence, a K_point of 5 is confirmed to be the optimum. Thus, the 5 x 5 x 5 K_point mesh was chosen for all the other supercells. Although higher values for the ecut and K_point mesh would have been chosen so as improve the accuracy of the calculations, it was noted that the higher values would have been more computationally expensive, considering the large number of atoms (108 atoms) that were modelled. However, the 50 Ry ecut and 5 x 5 x 5 Ry K_points are sufficient to give accurate results. Figure 4.1b shows a combined graph of all the alloys. From this graph, it is evident that A_91 takes the least energy of formation and hence, can easily be formed since it is the most mechanically stable. It can also be seen from the graphs that convergence is achieved when the ecut value is 50 Ry. Hence, this value is used throughout in our calculations.

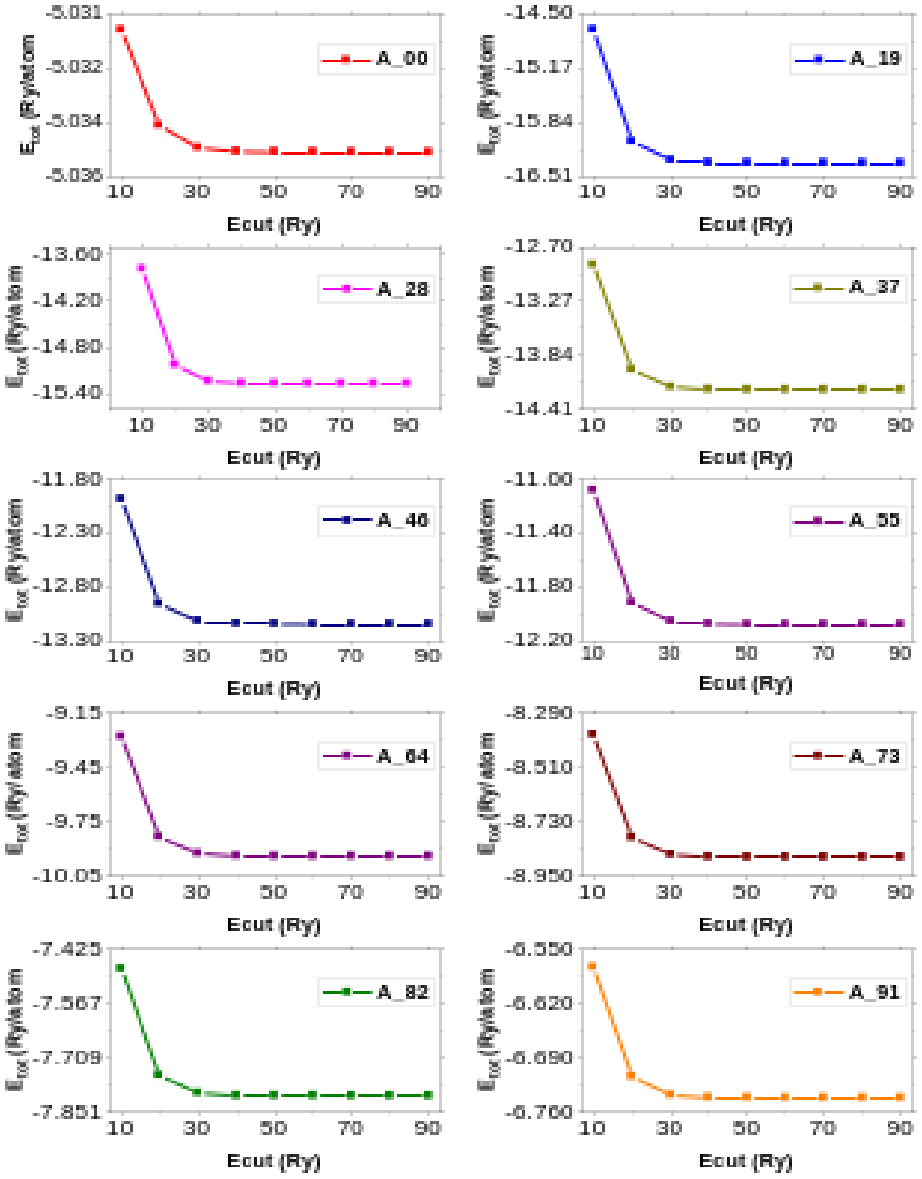

Figure 4. 1: Graphs of total energy per atom against ecut of each alloy.

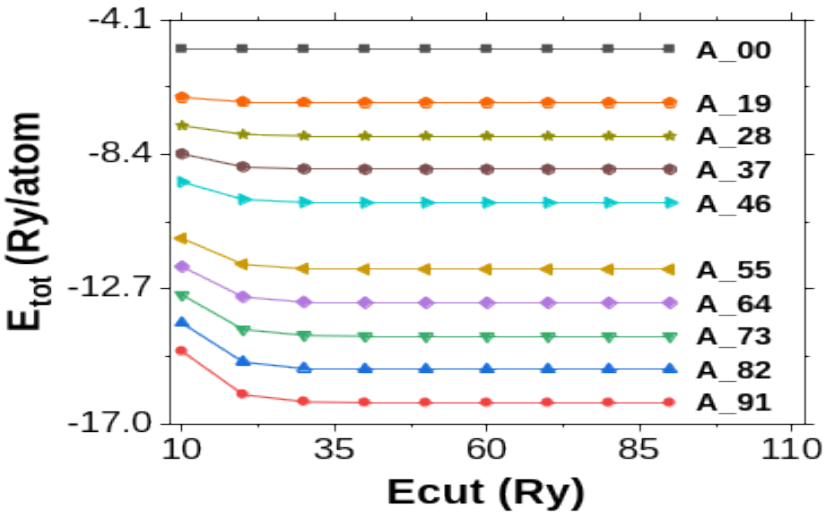

Figure 4. 2: Graphs of total energy per atom against ecut of all alloys combined

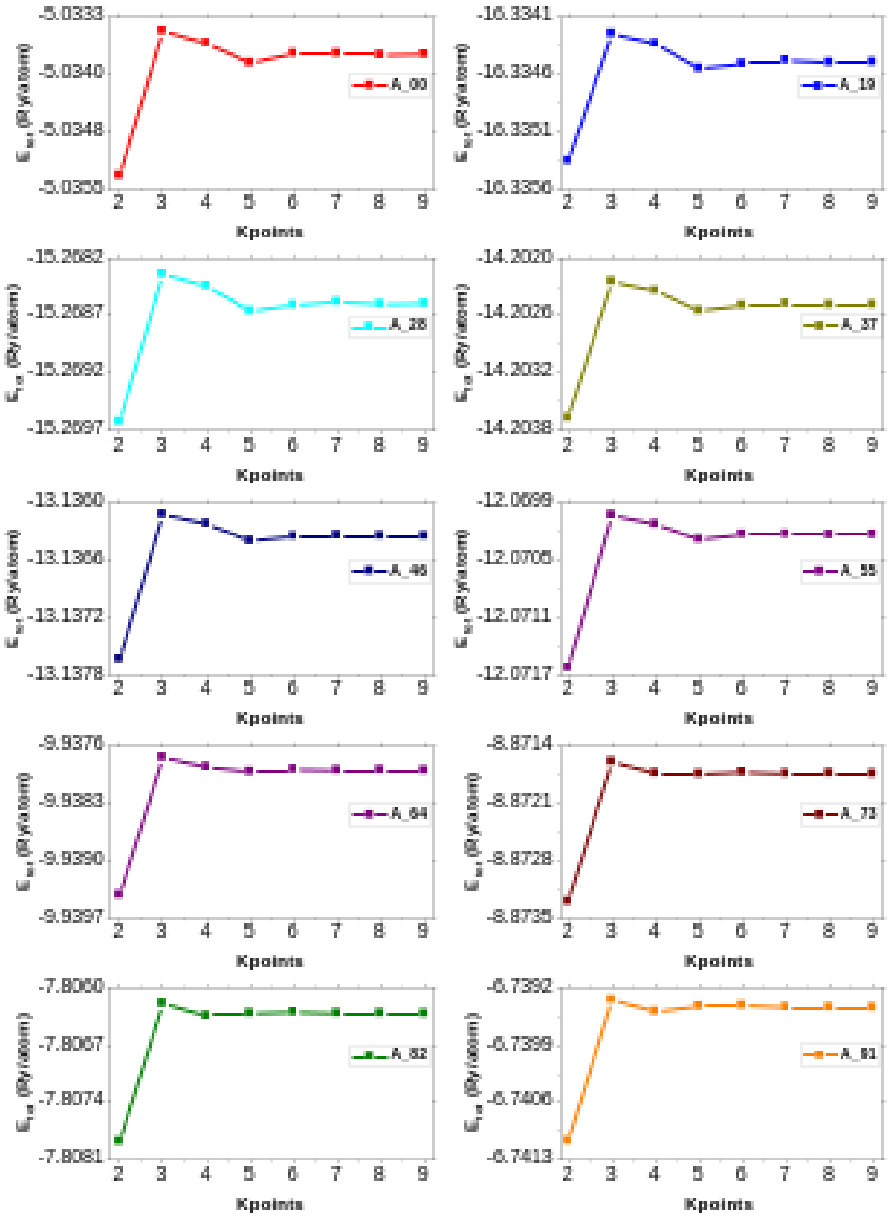

Figure 4. 3: Graphs of total energy per atom against K_points for each alloy

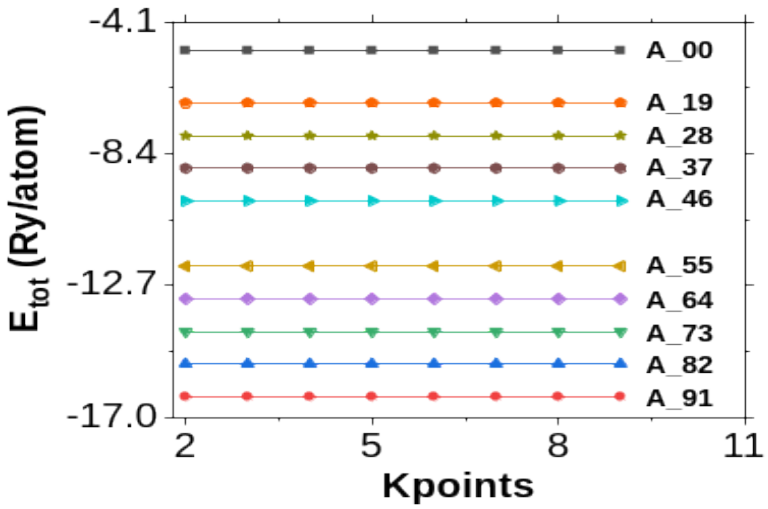

Figure 4. 4: Graphs of total energy per atom against K_points for all alloys combined.

The equilibrium volumes (V_o) of the alloys were obtained with the help of the third order Birch-Murnaghan equation of state (equation 3.1). From the graphs in figure 4.3, it can be noted that A_19 requires the least energy to be formed and therefore, the most stable. By applying the formula for finding the volume of a cube (equation 3.2), the volumes of the cells were calculated. It is evident from table 4.1 that the optimum lattice parameters reduce from A_19 to A_91. Since the trend from A_19 to A_91 is accompanied with an increase in the Si/Mg ratio, it implies that as the ratio increases, the lattice parameters of the alloys decrease. This shows that the unit cells shrink with increase in the Si/Mg ratio, and is in agreement with the corresponding consistent increase in the densities of the alloy samples.

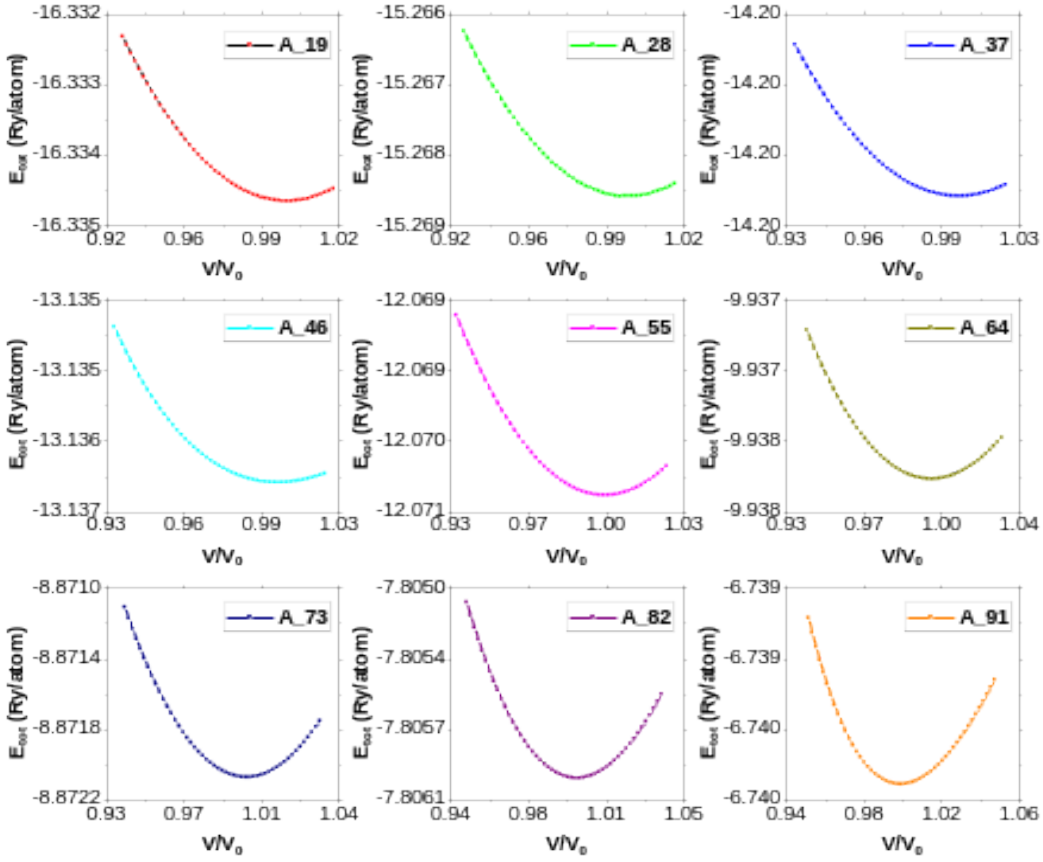

Figure 4. 5: Graphs of total energy per atom against normalized unit cell volume (V/Vo)

The density of 6060 T66 alloy obtained from literature is 2.7g/cm ^{3}, which is quite close to the values obtained in this study (Ambroziak & Solarczyk, 2018). It is evident that A_00 has the lowest density. The density of a material is a very important property of a material. It is related to the arrangement of atoms in the crystal, as well as the corresponding electron density (Daoud, Loucif et.al, 2012). The relatively high density of A_91 in this study shows the closeness of atoms in the crystal of A_91 as well as the high electron density in its structure.

Table 4. 1: The computed unit cell parameters and the densities of the nine alloy samples

Alloy sample	a (Å)	ρ (g/cm^3)
A_00	4.020	2.756
A_19	4.005	2.762
A_28	4.003	2.770
A_37	4.002	2.779
A_46	4.000	2.783
A_55	3.999	2.790
A_64	3.997	2.801
A_73	3.995	2.808
A_82	3.994	2.815
A_91	3.993	2.821
6060 T66		2.700 (**Ref**)

Ref - (Ambroziak & Solarczyk, 2018)

The lattice parameters obtained in this study compares favourably with those obtained for β", U1, and U2 precipitates by Froseth *et al*. (2003), which is 4.05 Å. Figure 4.4 shows the combined graph of the equilibrium lattice parameter and density against Si/Mg ratio, which shows that the reduction of the equilibrium unit cell parameter is not linear. The densities of the alloy samples (figure 4.4) on the other hand, increase non-linearly with Si/Mg ratio. At lower Si/Mg ratios, there is a sharp decrease in the unit cell parameters with a corresponding increase in the densities of the alloy samples.

At higher values of the Si/Mg ratios however, both the curves tend to a constant. This shows that as the Si/Mg ratio increases, the atoms are becoming smaller, which implies that as you move from A_19 to A_91, the atom sizes decrease. A_19 therefore, having the lowest density, will be the lightest and more appropriate for use in making aircraft parts. It is also worth noting that the difference between the highest (2.821 g/cm^3) and the lowest (2.762 g/cm^3) density is very small and hence, insignificant, since the difference between the masses of 1 cm^3 of A_19 and A_91 is 0.059g.

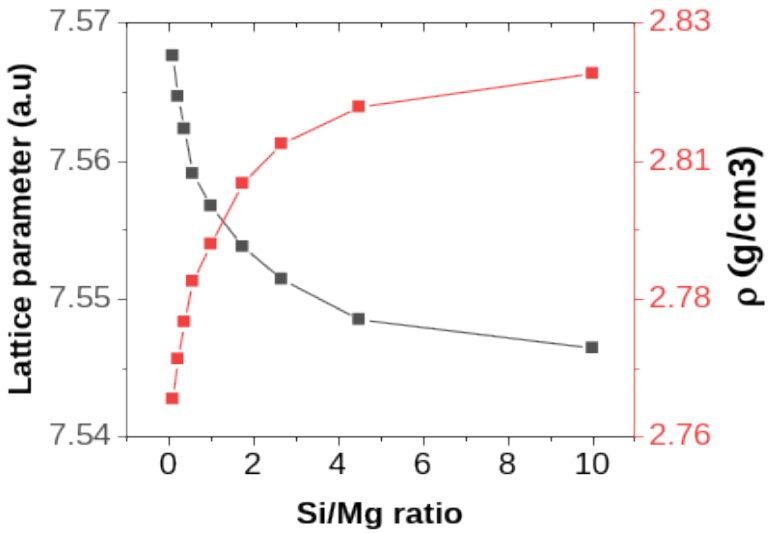

Figure 4. 6: Graphs of equilibrium unit cell parameters, and the densities of the alloy samples against Si/Mg ratio combined

4.3 Mechanical properties

Minor strains were introduced to the optimized unit cells during the computation of elastic constants. The minor distortions were implemented to ensure they stayed within the elastic limits of the crystal. Figures 4.5, 4.6, and 4.7 illustrate the stress-strain curves utilized to derive the elastic stiffness constants (c11, c12, and c44 respectively) for all the alloy samples. By performing a linear fit on the curves, the values of the elastic stiffness constants were obtained from the slopes. The fitted values are presented in table 4.2,

which shows that c_{11} decreases consistently from A_19 to A_46, after which it generally increases, likewise to c_{44}.

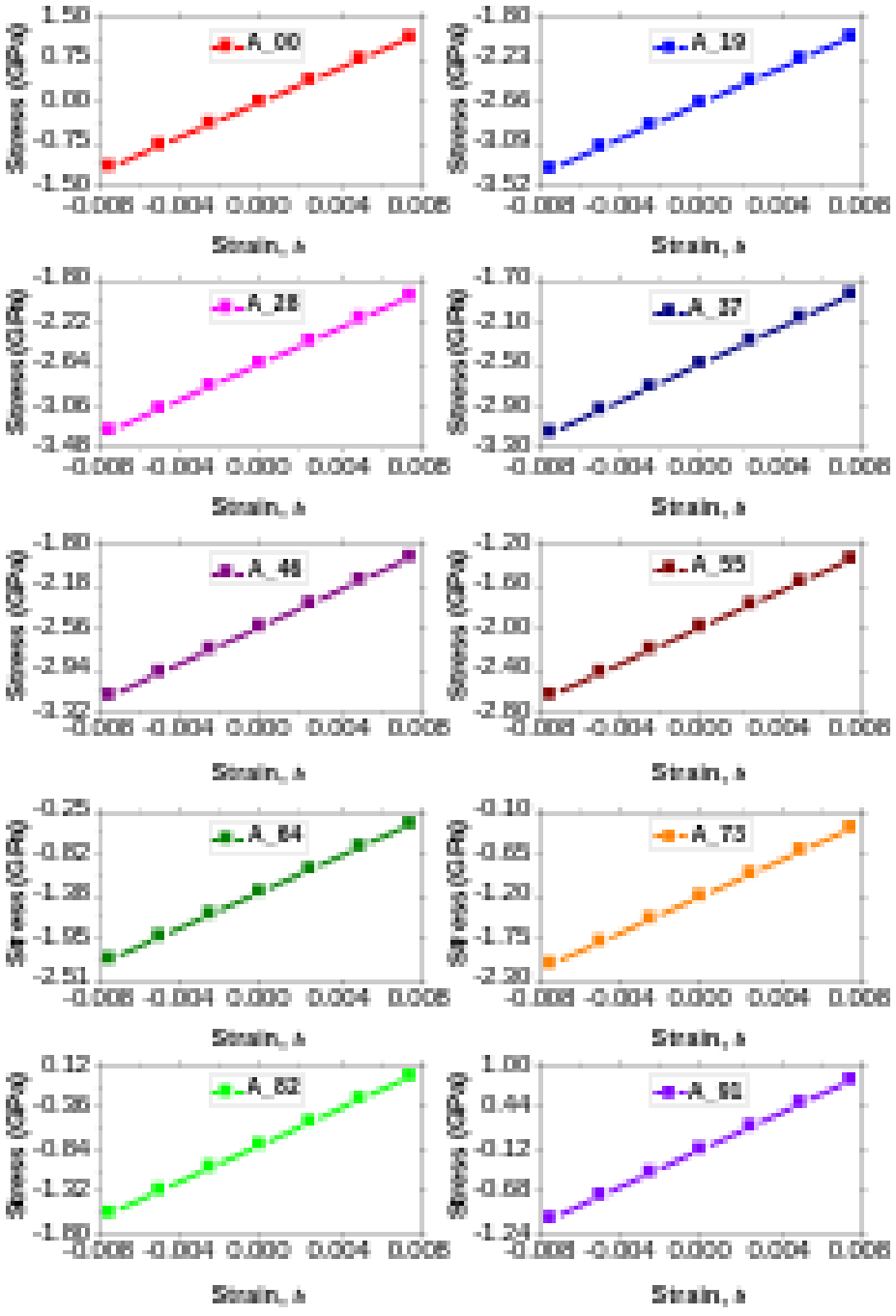

Figure 4. 7: The calculated stress-strain curves for elastic stiffness constant c11 for the cubic cell for all the samples.

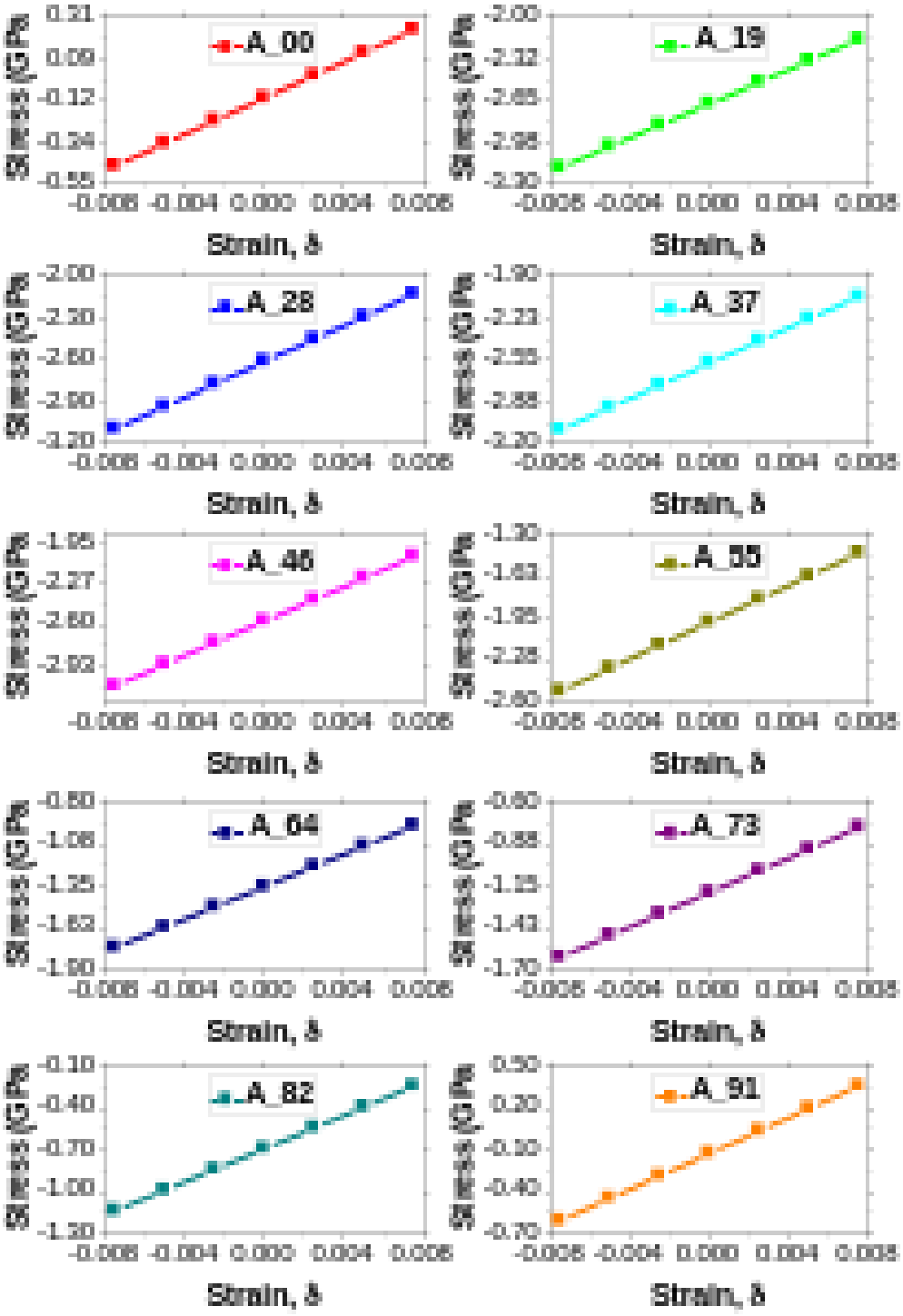

Figure 4. 8: The calculated stress-strain curves for elastic stiffness constant c12 for the cubic cells for all the samples

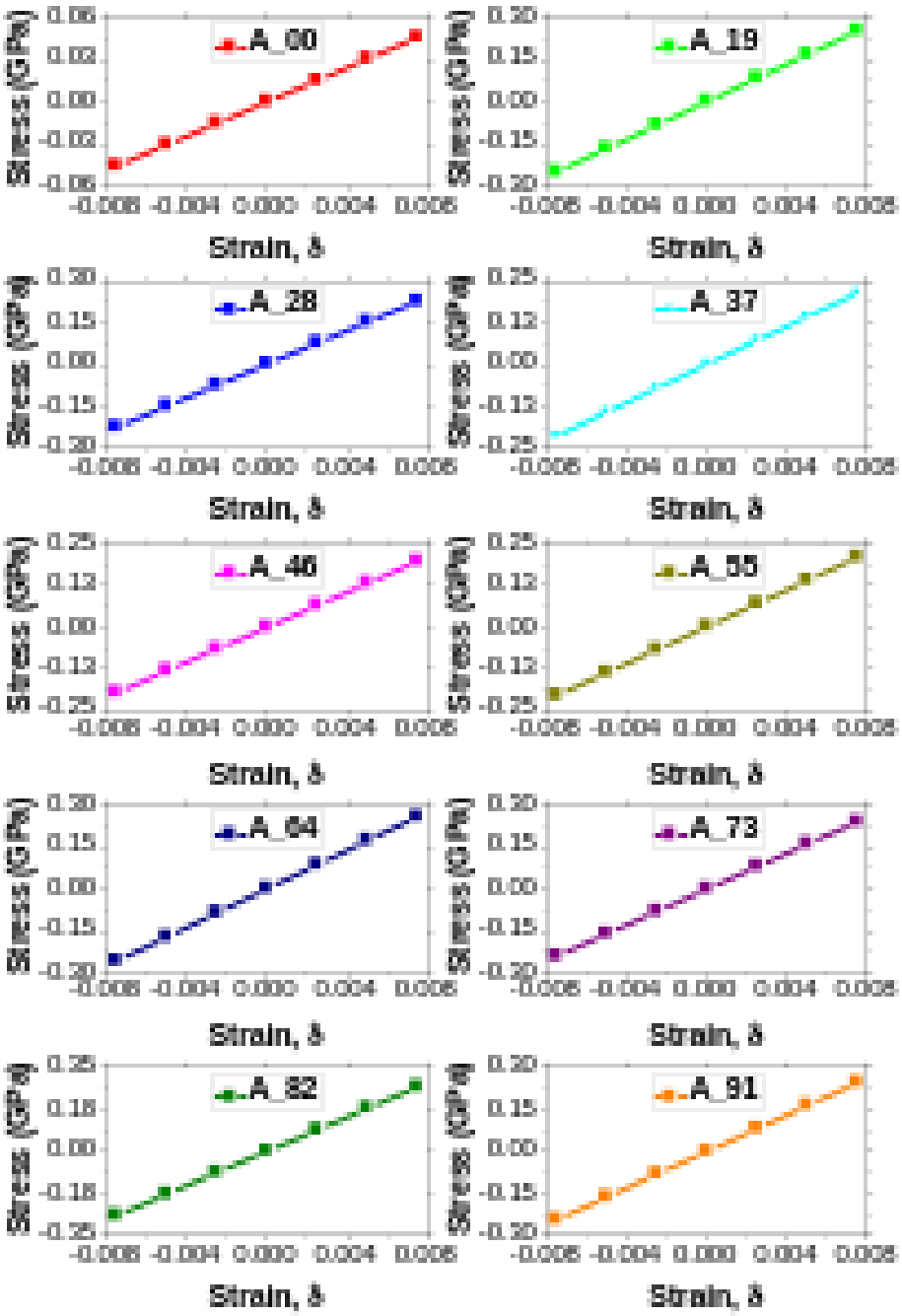

Figure 4. 9: The calculated stress-strain curves for elastic stiffness constant c44 for the cubic cell for all the samples

The values of the constants in the figures above were obtained from the distortion matrices D1 from the output file for c_{11} and c_{12}; and D2 for c_{44} as described earlier. The values were then plotted using Origin software, after which the linear fitting described above was done. The elastic stiffness constant c_{12} shows a consistent increase from A_19 to A_55, after which it generally decreases. The value of c_{12} for A_00 (pure aluminum supercell) is the lowest of all the samples, meaning that alloying increases the stiffness. The values of c_{11} and c_{44} for A_00 are generally within the range of the other samples with its c_{12} being the second highest after the value for A_91.

Table 4. 2: The calculated elastic stiffness constants (c11, c12 and c44) of the alloy samples

Alloy sample	c_{11} (GPa)	c_{12} (GPa)	c_{44} (Gpa)
A_00	100.5	62.5	34.6
A_19	90.5	68.0	33.2
A_28	87.8	69.5	29.5
A_37	87.0	69.9	29.5
A_46	82.5	71.0	24.5
A_55	88.6	71.5	29.6
A_64	114.3	61.8	34.4
A_73	118.2	59.9	34.2
A_82	126.3	58.7	34.8
A_91	123.3	63.3	33.2

The calculated values of all the elastic stiffness constants are positive, and hence, meet the Borne Huang criterion (Boucetta & Zegrar, 2013) as described in equation 3.8. This indicates that all the nine alloys are mechanically stable. c_{11} is related to elasticity of the length along the *a* direction (linear resistance to compression along the axes *a* direction),

c_{12} and c_{44} are related to the shape of the crystal. The values of $c_{11}>c_{12}>c_{44}$, which is an indication that the crystal is more susceptible to changes in shape than it is to changes in length since c_{11} is the largest.

Elastic constants control how materials react to external pressure. The crystalline elastic constants that can be described in the form of bulk modulus, shear modulus, Young's modulus and Poisson's ratio, are used to characterize engineering materials, and are useful parameters in the engineering design. The values of c_{11} drops from A_19 to A_46, then it starts to rise from A_55 up to A_82 then it reduces for A_91. This means that for lower Si/Mg ratio the value is higher and it starts reducing as the Si/Mg ratio increases up to where the ratio is 0.571, then it starts rising up to the point where the Si/Mg ratio is 4.5 and for Si/Mg ratio of 10, the value of c_{11} drops slightly. The value of c_{11} peaks at a Si/Mg ratio of 4.5.

The values of c_{12} increases from A_19 to A_55, then it starts to drop from A_64 up to A_82 and finally it rises slightly for A_91. The peak value of C_{12} is when the Si/Mg ratio is 1 (at A_55). The values of c_{44} drop from A_19 to A_46, then it starts to increase from A_55 up to A_82 then finally, it drops slightly. c_{44} peaks when the Si/Mg ratio is 4.5 and 0.1 (at A_82 and A_19). Generally, the values are in the order $c_{11}>c_{12}>c_{44}$. There is no overlap in the values of elastic stiffness constants, since the smallest value of c_{11} is higher than the highest value of c_{12}. Also, the smallest value of c_{12} is higher than the highest value of c_{44}.

The physical properties such anisotropic plastic deformation, elastic instability and crack behaviour, are significantly influenced by anisotropic factor A in the crystals (Chen, Yu, & Chiang, 2015). The shear anisotropic factor (A) must be equal to unity for an isotropic crystal. A_46 is more anisotropic than all the other alloy samples in this study since it's A deviates greatly from unity, while A_64 is the least anisotropic. The anisotropic factor is calculated using the formula in equation 3.16. The values of A are given in table 4.3.

Table 4. 3: Values of anisotropic factor (A) for the nine samples of Al-Mg-Si alloys

Alloy sample	A
A_00	1.821
A_19	1.476
A_28	1.612
A_37	1.725
A_46	2.130
A_55	1.731
A_64	0.655
A_73	0.586
A_82	0.514
A_91	0.553
AION	1.4(REF)

REF (Satapathy, et al., 2016)

The values of A obtained above compares fairly well with that of cubic aluminium oxynitride at ambient conditions which is 1.4 (Satapathy, et al., 2016). The above values of A show that all the nine alloy samples are anisotropic, since the values for each alloy is either less than unity or greater than unity. It is only when A=1 that the crystal is considered completely isotropic. Anisotropy is measured by how far the anisotropic

factor is from unity, such that when the anisotropic factor is far from unity the material is more anisotropic than the one whose anisotropic factor is near unity. A_46, therefore, has the highest value of A, meaning that it is the most anisotropic, since it also has the highest deviation from unity. The least anisotropic alloy is A_64 with an anisotropy factor of 0.655 which is only 0.345 away from unity.

Using the elastic stiffness constants (c_{ij}), the elastic constants (bulk modulus, shear modulus, Young's modulus and Poisson's ratio), and the mechanical properties (the Vickers hardness and the yield strength) were calculated. The values are presented in table 4.4.

Table 4. 4: The calculated elastic constants (bulk modulus (B), shear modulus (G), Young's modulus (E), Poisson ratio (μ), Pugh's ratio (n), Vickers hardness (Hv), and yield strength (Ys)) of the alloy samples. Hv and YS are in GPa, while μ and n do not have units

Alloy sample	B (GPa)	G (GPa)	E (Gpa)	μ	n	H_{vChen}	H_{vTian}	Y_s
A_00	74.0	27.6	73.1	0.335	2.70	1.35	3.14	4.05
A_19	75.5	21.5	59.0	0.370	3.51	-0.22	1.94	-0.67
A_28	75.6	18.5	51.3	0.387	4.09	-0.88	1.46	-2.64
A_37	75.6	18.0	50.1	0.390	4.20	-0.97	1.39	-2.92
A_46	74.8	13.8	39.0	0.413	5.42	-1.71	0.86	-5.14
A_55	77.2	18.0	50.2	0.392	4.28	-1.02	1.37	-3.05
A_64	79.3	30.9	82.0	0.328	2.57	1.93	3.57	5.80
A_73	79.3	32.1	84.6	0.322	2.48	2.27	3.82	6.80
A_82	81.2	34.4	90.4	0.315	2.36	2.79	4.24	8.38
A_91	83.3	31.9	84.8	0.330	2.61	1.93	3.58	5.78

The graph in figure 4.8 shows a slight decline in the bulk modulus for lower Si/Mg ratio and an increase in bulk modulus for higher Si/Mg ratios. The bulk modulus is at its highest when the Si/Mg ratio is 10. This shows that higher bulk modulus is achieved

when the Si/Mg ratio is higher. The bulk moduli obtained in this study, which ranges from 74.0-83.3 GPa compares favourably with the bulk modulus of 70 GPa, obtained for 6060 T66 alloy by Ambroziak & Solarczyk (2018). It also compares with those obtained by Froseth et al (Froseth, Hoier, Derlet, Andersen, & Marioara, 2003) which ranges from 65-71 GPa for the various precipitates of Al-Mg-Si alloys.

The improvement in the values of bulk modulus in this study is attributed to the enhanced alloying. There is an initial sharp decline in the shear moduli at lower Si/Mg ratios. As the Si/Mg ratio increases, the shear modulus also increases, and peaks at a ratio of 4.5, after which it decreases as the ratio increases further (figure 4.8). This means that to design an alloy that can withstand high shearing forces, the ratio of Si to Mg should be around 4.5. All the samples in this study have bulk moduli that are significantly greater than the shear moduli, which suggests that the alloys are more resistant to volume change than to shape change.

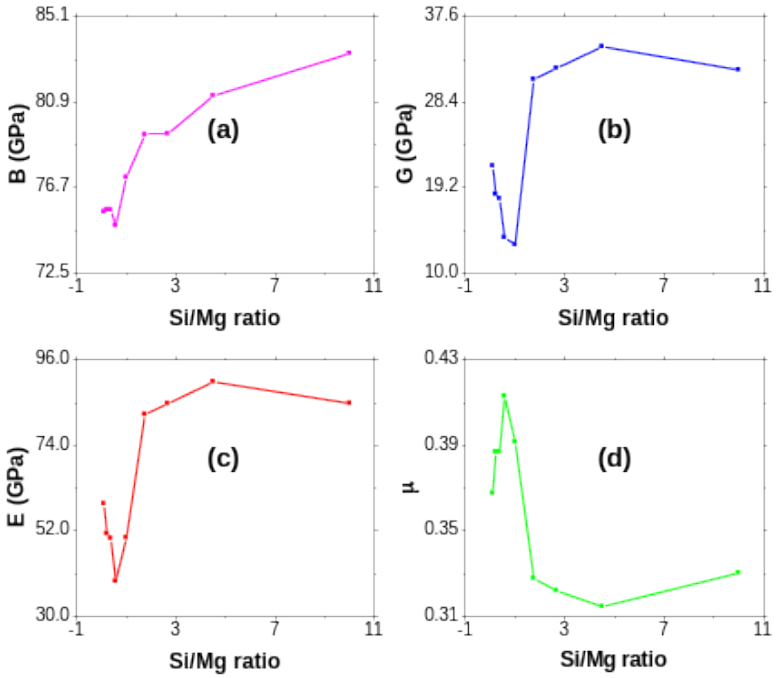

Figure 4. 10: The variations of the elastic constants (a. Bulk modulus, b. Shear modulus, c. Youngs modulus and d. Poisson's ratio) as a function of Si/Mg ratio

Young's modulus represents a critical mechanical property of materials that significantly influences industrial applications. The resistance of a material to longitudinal tension is measured by its Young's modulus. An increased Young's modulus signifies greater stiffness. Furthermore, Young's modulus influences a material's capacity to endure thermal shock, as it exhibits an inverse correlation with the critical thermal shock coefficient, which is essential for assessing a material's flammability. Figure 4.8(c) clearly demonstrates that the Young's modulus exhibits a trend consistent with that of the shear modulus for these alloys. A slight decrease in Young's modulus is observed for low Si/Mg ratio values, followed by a consistent increase in the modulus until it peaks at approximately a Si/Mg ratio of 4.5, which corresponds to alloy A_82. A_82 is suitable for components that necessitate high stiffness, such as the gearboxes in automobiles. An additional rise in the Si/Mg ratio results in a decrease in the value of Young's modulus.

Poisson's ratio serves as a valuable metric for evaluating various physical properties of solids, particularly in predicting stability against shear (Hadi, Rayhan, Naqib, Chroneous, & Islam, 2019). The Poisson's ratio values derived from this study align more closely with those reported by Ambroziak and Solarczyk for the 6060 T66 alloy, which was recorded as 0.3 (Ambroziak & Solarczyk, 2018). A reduced Poisson's ratio contributes to the enhanced stability of a material when subjected to shear forces. In this study, it is observed that the Poisson's ratio for all the alloys exceeds 0.3, indicating a tendency for

deformation. Among them, A_82 exhibits the lowest susceptibility to deformation, while A_28 demonstrates the highest susceptibility (figure 4.8).

Poisson's ratio serves as a valuable metric for evaluating various physical properties of solids, particularly in predicting stability against shear (Hadi, Rayhan, Naqib, Chroneous, & Islam, 2019). The Poisson's ratio values derived from this study align more closely with those reported by Ambroziak and Solarczyk for the 6060 T66 alloy, which was recorded as 0.3 (Ambroziak & Solarczyk, 2018). A reduced Poisson's ratio contributes to the enhanced stability of a material when subjected to shear forces. In this study, it is observed that the Poisson's ratio for all the alloys exceeds 0.3, indicating a tendency for deformation. Among them, A_82 exhibits the lowest susceptibility to deformation, while A_28 demonstrates the highest susceptibility (figure 4.8). The higher the value, the more ductile the material. All the values of Poisson's ratios above are more than 0.27 hence, the alloys are ductile. The Poisson's ratio rises at low Si/Mg ratio then falls approaching a low almost asymptotic value before rising steadily with a further increase in the Si/Mg ratio.

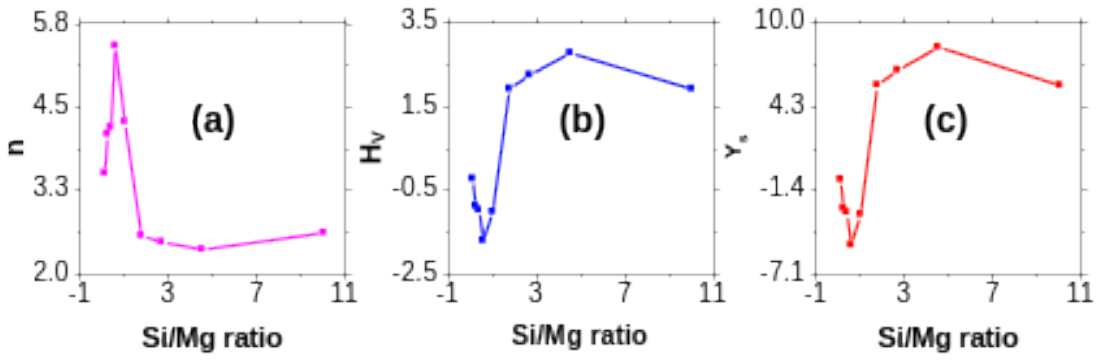

Figure 4. 11: The variations of (a) Pugh's ratio (b) Vickers hardness (c) Yield strength as functions of Si/Mg ratio

Pugh's ratio (Pugh, 1954) confirms the ductility or brittleness of all the alloys. A material is ductile if the Pugh's ratio is greater than 1.75. The Pugh's ratios obtained in this study are greater than 1.75 for all the nine alloys, confirming that the alloys are ductile (figure 4.5b). This means that the materials are flexible and can be beaten into thin sheets, which is a crucial property of materials for technical and industrial applications. The values of Pugh's ratio obtained in this study at 2.57-5.42 (table 4.4) shows that all the alloys in this study are ductile materials with A_46 being the most ductile, and A_82 being the least ductile. Although the alloys in this study are ductile based on Pugh's and Poisson ratio, this criterion alone is not sufficient to suggest specific applications of these alloys in the industry since it leads to elongation to fracture (ELF) in a tensile test which are only in the regime of a few percent (less than recommended 10% ELF) of plastic deformation.

Hardness is another crucial property that influences numerous industrial applications of materials. The resistance exhibited by a material to external mechanical actions is a critical factor, as it influences the extent to which scratching, abrasion, indentation, or other permanent alterations can impact its surface integrity. Hard materials like diamond exhibit low compressibility and high wear resistance (Manyali & Sifuna, 2019), characteristics that are particularly advantageous in the manufacturing of automotive components, such as aircraft skins, that require durability and longevity. Materials exhibiting a Vicker's hardness exceeding 40 GPa are classified as super hard materials (Teter, 1998). The alloys examined in this study exhibit a tendency towards softness, as evidenced by the maximum hardness value of 2.79 GPa for alloy A_82 according to the Chen model, and 4.24 GPa as per the Tian model. The hardness values for Al-Mg-Si alloys remain significantly elevated. The overestimation of hardness values for soft materials in this study can be attributed to the Chen and Tian models utilized, which are recognized for this tendency in macroscopic modeling (Avery, et al., 2019). The negative

values observed in the Chen model arise from the presence of a negative term (-3) in equation (11). Consequently, if the first term of the equation produces a value lower than 3, it results in a negative hardness value. The Chen model is recognized for its accurate predictions regarding the hardness of super hard materials; however, it produces negative values for softer materials with hardness below 5 GPa (Avery, et al., 2019). A_82 is thus advised for application in plane skins due to its superior hardness compared to all other alloys.

Vickers hardness falls first as the Si/Mg ratio is increased from zero before rising to a maximum value and then falling again slightly (figure 4.5b). Precipitation is delayed in Mg-rich alloys (lower Si/Mg ratios) and hence, the low hardness values at low ratios (Mageto, 2003). The increase in hardness is due to more β” precipitates which are responsible for coarser structures in 6xxx series and hence, a higher hardness. It is however worth noting that the increase in the Vickers hardness with Si/Mg ratio has a limit, it peaks when the Si/Mg ratio is at 4.5 (alloy A_82), after which it generally drops.

The Vickers hardness for the pure aluminum (A_00) is 1.35GPa from Chen model and 3.14 GPa from Tian model. The values of Hv for Si/Mg ratio of one and below are negative while for Si/Mg ratios above 1, the Hv is higher than that of pure aluminum. This implies that for higher Vickers hardness to be achieved, the amount of Silicon used in alloy should be higher than the amount of magnesium used with the peak being when the amount of Si is 4.5 times the amount of magnesium. The negative in some values of Vickers hardness can be ignored since Vickers hardness is a scalar quantity hence the negative has no meaning.

The calculation of yield strength is performed using the formula presented in equation 3.15, where HV represents the Vickers hardness and YS denotes the yield strength (Mageto, 2003). The data indicates a direct proportionality between the yield strength of the alloys and their Vickers hardness. The yield strength adheres to the Hall-Petch equation, indicating that a decrease in grain size results in an increase in the strength of the alloy (figure 4.5c) (Whang, 2011). The graph depicting density in relation to the Si/Mg ratio indicates a positive correlation, where density increases as the Si/Mg ratio rises. An increase in density indicates a decrease in the size (volume) of the crystal or grain size. Therefore, for these alloys, a higher Si/Mg ratio results in a decrease in grain size, which in turn leads to an increase in yield strength.

CHAPTER FIVE:

CONCLUSIONS AND RECOMMENDATIONS

5.1: Conclusions

The study has successfully modeled the structures of Al-Mg-Si alloys at different concentrations of aluminum, magnesium, and silicon using Burai software. The structures modeled were stable under ambient conditions (since they meet the Borne-Huang criterion) meaning that the alloys can be fabricated experimentally.

This study has also investigated some mechanical properties of Al-Mg-Si alloys at different concentrations of Al, Mg, and Si using first-principles calculations based on DFT. We have computed the bulk modulus, shear modulus, Young's modulus, Poisson's ratio, Pugh's ratio, and elastic anisotropy constant factor independently for the nine alloys. The values of Poisson's ratio and Pugh's ratio suggest that all nine alloys are ductile/flexible. The results of elastic stiffness constants reveal that the alloys are mechanically stable and have significant anisotropy in terms of elasticity and flexibility.

It is evident from this study that Si/Mg ratio is a critical factor when it comes to Al-Mg-Si alloys. The optimum Si/Mg ratio for most of the mechanical properties is 4.5. All the values of the anisotropic factor (A) show that the alloys are highly anisotropic since none of the values is unity. Young's modulus increases with an increase in Si/Mg ratio peaking when the Si/Mg ratio is 4.5 before starting to drop. Poisson's and Pugh's ratios both decrease with an increase in Si/Mg ratio hitting its lowest (minimum) value when the Si/Mg ratio is 4.5. Vickers hardness and Yield strength increase with the increase in Si/Mg ratio both peaking when the value of Si/Mg ratio is 4.5 before decreasing with a further increase in Si/Mg ratio.

5.2: Recommendations for further work

The results can be improved by improving the modelling techniques used in this study. Atoms could be replaced using an algorithm instead of doing manually like was done in this study.

The alloys studied so far can be applied in manufacture of parts of airplanes owing to their relatively low densities and their high hardness, especially in plane skins. The ductility criterion used in this study (Pugh's ratio) does not allow for recommendations for industrial applications since it leads to an elongation to fracture percentage of less than 10. The high yield strengths of these alloys also make them suitable to be used for making pylons for power transmission and towers.

Si/Mg ratio studied here is not conclusive and is not the only determinant of the mechanical properties of Al-Mg-Si alloys. Further research is recommended on heat treatments of the alloys studied so far so as to further improve the mechanical properties of the alloys in this study.

REFERENCES

Adllan, A., & Corso, A. (2011). Ultrasoft pseudopotentials and projector augmented-wave data sets: Application to diatomite molecules. *Journal of Physics: Condensed Matter, 23*(42), 425501. Retrieved from https://doi.org/10.1088/0953-8984/23/42/425501.

Ambroziak, A., & Solarczyk, M. (2018). *Application and mechanical properties of aluminium alloys.* Gdansk: Gdansk University of Technology, Faculty of Civil and Environmental Engineering. doi:10.1201/9781315166605-121

Avery, P., Wang, X., Oses, C., Gossett, E., Proserpio, D. M., Toher, C., Zurek, E. (2019). Predicting superhard materials via a machine learning-informed evolutionary structure search. *computational materials, 5*(89). doi:https://doi.org/10.1038/s41524-019-0226-8

Baruah, M., & Borah, A. (2020). Processing and precipitation strengthening of 6xxx series aluminium alloys: A review. *International Journal of Material Science, 1*(1), 40-48. doi:10.22271/27078221.2020.v1.ila.10.

Bon, M., & Oppenheimer, R. (1927). On the quantum theory of molecules. *Annalen der Physik*, 457-484.

Boucetta, S., & Zegrar, F. (2013). Density Functional Study of elastic, mechanical and thermodynamic properties of MgCu with a CsCl-type structure. *Journal of Magnessium and Alloys 1*, 128-133.

Bouchenafa, M., Benmakhlouf, A., Sidoumou, M., Bouchemadou, A., Maabed, S., & Halit, M. (2020). Theoretical Investigation of the structural, elastic, electronic and optical properties of the ternary tetragonal tellurides KBTe2 (B=Al,In). *Materials Science in Semiconductor Processing*, 1-9.

Bruno, V., & Nicholas, L. (2021, December 14). Visualizing the abundance of elements in the Earth's crust. *Future of the environment*, 205.

Chen, W.-H., Yu, C.-F., & Chiang, H.-C. (2015). First principles density functional calculations of physical properties of orthorhombic Au2Al. *Intermetallics, 62*, 60-68.

Chen, X., Niu, H., Franchini, C., Li, D., & Li, Y. (2011). Hardness of T-carbon: Density Functional Calculations. *Physical Review B, 84(12)*, 121405.

Derlet, P., Andersen, S., Marioara, C., & Froseth, A. (2009). A first Principles Study of the B''-phase in Al-Mg-Si alloys. *Journal of Physics: Condensed Matter*, 4011.

Fleury, E., & Kim, D. (2008, February). Poisson's ratio and fragility of bulk metallic glasses. *Journal of Materials Research*, 101-105. doi:10.1557/JMR.2008.0060

Franco, P., Jona, Paul, M., & Marcus. (2006). Lattice parameters of aluminum in Mbar range by first principles. *Journal of Physics: Condensed Matter, 18*, 10881-10888.

Froseth, A., Hoier, R., Derlet, P., Andersen, S., & Marioara, C. (2003). Bonding in MgSi and Al-Mg-Si compounds relevant in Al-Mg-Si alloys. *Physical Review B, 67*, 224106.

Hadi, M., Rayhan, M., Naqib, S., Chroneous, A., & Islam, A. (2019). Structural, elastic, thermal, and lattice dynamic properties of new 321 MAX phases. *Computational Material Science, 170*(1019144), 1-9.

Hill, R. (1952). *Proceedings of the Physical Society A, A65*, **349**. https://doi.org/10.1088/0370-1298/65/5/307

Jackoben, J. (2016). *Microstructure and mechanical properties of welded AA6082 aluminum alloys.* Trondeheim, Noway: Norwegian University of Science and Technology, M. Sc thesis.

Kiely, E., Zware, R., Fox, R., Reilly, A., & Guerin, S. (2021). Density functional theory predictions of the mechanical properties of crystalline materials. *Royal Society of Chemistry, 23*, 5697-5710.

Kohn, W., & Sham, L. (1965). Self-Consistent Equations Including Exchange and Correlation Effects. *Physical Review. 140 (4A)*, 1133.

Landau, L., & Lifshitz, E. (1970). *Theory of Elasticity Course of Theoretical Physics (3rd Ed, Vol. 7).* Oxford: Butterworth-Heinemann.

Lejaeghere, K., Bihlmayer, G., Bjorkman, T., Blaha, P., & Blugel, S. (2016). Reproducibility in Density Functional Theory Calculations of Solids. *Science, 351(6280)*, 3000.

Mageto, J. M. (2003). TEM study of microstructure in relation to hardness and ductility in Al-Mg-Si alloys (6xxx series). MSC Thesis. Department of Physics, Faculty of Natural Sciences and Technology, Norwegian University of Science and Technology (NTNU)

Manyali, G., & Sifuna, J. (2019). Low Compressible BP3N6. *AIP Advances, 9*(125929), 1-5. Retrieved from https://doi.org/10.10363/1.5129268

Marie, H. (2021, February 17). Retrieved from What Is Shear Modulus?: https://www.thoughtco.com/shear-modulus-4176406

Marioara, C., Andersen, S., Zandbergen, H., & Holmestad, R. (2005). *The Influence of Alloy Composition on Precipitate of the Al-Mg-Si System* . Retrieved from http://www.sintef.no/norlight/ProjectPortfolio/HeatTreatmentFundamental

Naturfosch, Z. (1977). Pseudopotential Theory of Molecules. New York: University of New York.

Ninive, P., Strandlie, A., Grubandsen-Dahl, S., Lefebvre, W., & Marioara, C. D. (2014). Detailed Atomistic Insight into B"-Phase in Al-Mg-Si alloys. *Acta Materialia 69*, 126-134.

Ongwen, N., Ogam, E., & Otunga, H. (2020). Ab initio study of elastic properties of Orthorhombic Cadmium Stannate as a substrate for manufacture of MEMS devices. *Materials Today Communications*, 101822.

Pugh, S. (1954). XCII. Relations between the elastic moduli and the plastic properties of polycrystalline pure metals. *The London, Edinburg and Dublin Philosophical Journal of Science, 84*(367), 823-843. Retrieved from https://doi.org/10.1080/14786440808520496.

Ravindran, P., Fast, L., Korzhavyi, P., Johnson, B., Wills, J., & Ericksson, O. (1998). Density functional theory for calculation of elastic properties of orthorhombic crystals: Application in TiSi2. *Journal of Applied Physics, 84*(9), 4891-4904.

Saidi, A., & Kahoro, S. (2001). Re: Experience of road traffic accident victims at the Nairobi Hospital. *East African Medical journal, 79*(4), 175.

Satapathy, S., Muhtar , A., Dattatraya, D., Russell, J. H., Brian, S., & Petro, K. (2016). Singe-crystal elastic properties of aluminium oxynitride (AION) from brillouin scattering. *Journal of American Ceramic Society, 99*(4). Retrieved from https://doi.org/10.1111/jace.14065

Schwerdfeger, P. (2011). The Pseudopotential approximation in electronic structure theory. *Physical Chemistry, 12*(17), 1-9. Retrieved from https://10.1002/cphc.201100387

Teter, D. (1998). Computational alchemy: The search for new super hard materials. *MRS Bulletin, 23*(1), 22-27. Retrieved from https://doi.org/10.1557/S0883769400031420

Vanderbilt, D. (1990). Soft self-consistent pseudopotential in generalised eigenvalue formalism. *Physical Review B: American Physical Society., 41*(11), 7892-7895. Retrieved from https://doi.org/10.1103/PhyRevB.41.7892

Wen, Y., Wang, L., Liu, H., & Song, L. (2017). Ab initio Study of elastic and mechanical properties of B19 TiAl. *Crystals 7(39)*, 1-11.

Werinos, M., Antrekowisch, H., Ebner, T., Prillhofer, R., Uggowitzer, P. J., & Pogatscher, S. (2016). Hradening of Al-Mg-Si alloys: Effects of trace elements and prolonged natural aging. *Materials and Design, 107*, 257-268.

Whang, S., (2011). Nanostructured metals and alloys. *Science Direct*.

WHO. (2022). *Powered two- and three-wheeler safety; a road safety for decision-makers and practitioners.* Geneva: WHO.

Yuan, W., Liang, Z., Zhang, C., & Wei, L. (2012). Effects of La addition on the mechanical properties and thermal-resistant properties of Al-Mg-Si-Zr alloys based on AA6201. *Material and Design, 34*, 788-792.

Zener, C. (1948). *Elasticity and anelasticity of metals.* Chicago: University of Chicago, USA

Gates, D. (2023). Final report on Boeing 737 MAX crash sparks dispute. *The Seattle Times.*

Katsura, T., Tange, Y., (2019). A simple derivation Birch-Murnaghan EOSs,. *Minerals*,9,745

APPENDICES

Appendix 1: A sample input file

```
&CONTROL
   calculation = "scf"
   max_seconds =  8.64000e+04
   outdir      = "./tmp"
   prefix      = "Al"
   pseudo_dir  = "./"
   tprnfor     = .TRUE.
   tstress     = .TRUE.
/
&SYSTEM
   celldm(1)       =  20.548960
   degauss     =  1.00000e-02
```

```
   ecutrho     =  80
   ecutwfc     =  10
   ibrav       = 1
   nat         = 64
   ntyp        = 3
   occupations = "smearing"
   smearing    = "gaussian"
/
&ELECTRONS
   conv_thr        =  1.00000e-10
   electron_maxstep = 200
   mixing_beta     =  7.00000e-01
   startingpot     = "atomic"
   startingwfc     = "atomic+random"
/
K_POINTS {automatic}
2 2 2 0 0 0
ATOMIC_SPECIES
Si     28.08550  Si.pbesol-n-rrkjus_psl.1.0.0.UPF
Mg     24.30500  Mg.pbesol-spnl-rrkjus_psl.1.0.0.UPF
Al     26.98154  Al.pbesol-nl-rrkjus_psl.1.0.0.UPF

ATOMIC_POSITIONS {angstrom}
Al      0.000000   0.000000   2.717592
Al      1.358795   4.076389   1.358795
Al      2.717592   0.000000   0.000000
Al      4.076389   4.076389   4.076389
Al      0.000000   2.717592   0.000000
Al      1.358795   1.358795   4.076389
```

Al	2.717592	2.717592	2.717592
Al	4.076389	1.358795	1.358795
Al	0.000000	0.000000	8.152777
Al	1.358795	4.076389	6.793981
Al	2.717592	0.000000	5.435185
Al	4.076389	4.076389	9.511574
Al	0.000000	2.717592	5.435185
Al	1.358795	1.358795	9.511574
Al	2.717592	2.717592	8.152777
Al	4.076389	1.358795	6.793981
Al	0.000000	5.435185	2.717592
Al	1.358795	9.511574	1.358795
Al	2.717592	5.435185	0.000000
Al	4.076389	9.511574	4.076389
Al	0.000000	8.152777	0.000000
Al	1.358795	6.793981	4.076389
Al	2.717592	8.152777	2.717592
Al	4.076389	6.793981	1.358795
Al	0.000000	5.435185	8.152777
Al	1.358795	9.511574	6.793981
Al	2.717592	5.435185	5.435185
Al	4.076389	9.511574	9.511574
Al	0.000000	8.152777	5.435185
Al	1.358795	6.793981	9.511574
Al	2.717592	8.152777	8.152777
Al	4.076389	6.793981	6.793981
Al	5.435185	0.000000	2.717592
Si	6.793981	4.076389	1.358795
Al	8.152777	0.000000	0.000000

Al	9.511574	4.076389	4.076389
Al	5.435185	2.717592	0.000000
Al	6.793981	1.358795	4.076389
Al	8.152777	2.717592	2.717592
Al	9.511574	1.358795	1.358795
Al	5.435185	0.000000	8.152777
Al	6.793981	4.076389	6.793981
Al	8.152777	0.000000	5.435185
Al	9.511574	4.076389	9.511574
Al	5.435185	2.717592	5.435185
Al	6.793981	1.358795	9.511574
Al	8.152777	2.717592	8.152777
Al	9.511574	1.358795	6.793981
Al	5.435185	5.435185	2.717592
Al	6.793981	9.511574	1.358795
Al	8.152777	5.435185	0.000000
Al	9.511574	9.511574	4.076389
Al	5.435185	8.152777	0.000000
Al	6.793981	6.793981	4.076389
Al	8.152777	8.152777	2.717592
Al	9.511574	6.793981	1.358795
Mg	5.435185	5.435185	8.152777
Al	6.793981	9.511574	6.793981
Al	8.152777	5.435185	5.435185
Al	9.511574	9.511574	9.511574
Al	5.435185	8.152777	5.435185
Al	6.793981	6.793981	9.511574
Al	8.152777	8.152777	8.152777
Al	9.511574	6.793981	6.793981